Paulo José Duarte Neto

Multifractal Analysis of Closed Contour Fluctuations

UNIVERSIDADE FEDERAL RURAL DE PERNAMBUCO

PRÓ-REITORIA DE PESQUISA E PÓS-GRADUAÇÃO

PROGRAMA DE PÓS-GRADUAÇÃO EM BIOMETRIA E ESTATÍSTICA APLICADA

UNIVERSITY OF ANTWERP

DOCTORAL STUDY PROGRAMME

Multifractal Analysis of Closed Contour Fluctuations

Thesis presented to the Programa de Pós-Graduação em Biometria e Estatística Aplicada of UFRPE and the Doctoral Study Programme of University of Antwerp as partial requirement to award the joint doctorate title.

Concentration field: Statistical and Computational Modeling

Advisor (UFRPE): Prof. Dr. Borko Stosic

Advisor (University of Antwerp): Prof. Dr. Milorad Milosevic

RECIFE-PE - DEC/2012.

Ficha catalográfica

UNIVERSIDADE FEDERAL RURAL DE PERNAMBUCO

PRÓ-REITORIA DE PESQUISA E PÓS-GRADUAÇÃO

PROGRAMA DE PÓS-GRADUAÇÃO EM BIOMETRIA E ESTATÍSTICA APLICADA

UNIVERSITY OF ANTWERP

DOCTORAL STUDY PROGRAMME

Multifractal Analysis of Closed Contour Fluctuations

Paulo José Duarte Neto

Thesis considered suitable to award the joint doctorate title in Biometria e Estatística Aplicada by the UFRPE and in Science by the University of Antwerp, defended and unanimity approved by the follow exam committee

Advisors:

Prof. Dr. Borko Stosic
Deinfo/Universidade Federal Rural de Pernambuco

Prof. Dr. Milorad Milosevic
NANO CoE/University of Antwerp

Exam Committee:

Prof. Wilson Rosa de Oliveira Junior
Deinfo/Universidade Federal Rural de Pernambuco

Prof. Dr. Pedro Hugo de Figueirêdo
DF/Universidade Federal Rural de Pernambuco

Prof. Dr. Ivon Palmeira Fittipaldi
ReNE/MCTI

To Professor Dr. Eufrázio de Souza Santos

Acknowledgments

First of all, thank God for a blessed and beautiful life, and for the health and energy that you have given me to reach all of my professional expectations till now.

In 1998, I started undergraduate studies in Fish Engineering at the Universidade Federal Rural de Pernambuco, and since that time, mirroring in all professors that composed that course, my aspirations to be a professor and a researcher of an university have started. I never deviated from this goal and now, finishing this last academic task, already as a professor of the same university, I am feeling in debt with everyone (including all personal staff of the Departamento de Pesca, Departamento de Biometria e Estatística Aplicada and Unidade Acadêmica de Garanhuns) that contributed with knowledge, words of support, and motivation to reach my professional dreams. Specially, I would like to thank to the people of the DIMAR lab, where I spent 6 wonderful years of my life as an undergraduated and a master degree student.

From the DIMAR lab, I would like to thank to Prof. Dr. Francisco Santana for the otolith images of *Mugil curema* and for your special friendship. Also to Prof. Dr. Rosangela Lessa, who I consider as one of the responsible for my professional conquests and as my "scientific mother". Thank you for your rich advices and teaching during this long way.

I am immensely grateful to the doctoral students and researchers of the Condensed Matter Theory group, who provided me significant contributions and support to my research activities at The University of Antwerp, and a pleasant stay in Belgium. To Prof. Dr. Milorad Milosevic for the opportunity to work with him and his group and for his precious contributions to my thesis and to my professional consolidation as a researcher.

To my student colleagues of the Doctoral Programme in Biometrics and Applied Statistics for the friendship and mutual collaboration during these 4 hard years, in special to my friend Gabriel Rivas. To Prof. Dr. Tatijana Stosic for the support and knowledge that she gave me in fractal and multifractal field. My thesis was born in her classes, for which I am very grateful to her.

I would like to thank to my family, Ana Cristina, Alexandre e Cristiana, to the support and comprehension during the difficult days. To my beloved Leila for her patience and

comprehension of the importance of this time for us. Far or close, we will always be together.

Finaly, Prof. Dr. Borko Stosic, thank you for the opportunity to work with you and for sharing with me your experiences and knowledge. Be sure that your wise advices, sometimes as a advisor, sometimes as a "Master Jedi", and sometimes as a father and friend, made me a better person in all senses. Thank you very much for your kindness and patience.

"*Only different in your mind. You must unlearn what you have learned.*"

Yoda

Abstract

In recent decades multifractal analysis has been successfully applied to characterize the complex temporal and spatial organization of diverse natural phenomena such as heartbeat dynamics, the dendritic shape of neurons, retinal vessels, rock fractures, etc. However, common methods of multifractal analysis do not seem appropriate for analyzing quasi-one-dimensional structures, with complexity far from filling two dimensional space, but more complex than a line, such as the contours of objects. For this reason, the characterization of multifractal properties of closed contours has up to date remained rather elusive. Here a new, robust, technique, "The Traveling Observer" Multifractal Detrended Fluctuation Analysis is presented, which bridges the gap between the methods used for geometrical fractals and those used for temporal series, reducing the limitations present in existing multifractal techniques to analyze contours. The procedure first maps the contour onto a "time series" of distances from the central path (defined by harmonic term zero), as observed by a virtual observer traveling along this path at constant angular speed. The fluctuations from the central path of the contour perimeter are registered as a "time series", and the MF-DFA is then implemented to quantify the "temporal" correlations of this series. The relevance of studying the fractal properties of the contour fluctuations is demonstrated through several applications to natural and simulated data, highlighting the advantages of this new approach. The results indicate that the new procedure can capture intrinsic characteristics of the growth process hidden in the contour fluctuations, that are reflected by the multifractal parameters. In fact, these parameters can be used as shape descriptors in classification problems, as is practice with other traditional quantitative methods employed for shape analysis. On the other hand, their interpretation goes beyond simple shape classification, uncovering meaningful and sometimes unexpected features about natural structures and their growth. For instance, relationships between multifractal features of otolith contour fluctuations and fish size and age at maturity has been observed, and properties of agregates generated through a computational model at different growth conditions are shown to have close correspondence with thermodynamic behavior of magnetic model systems.

Keywords: Multifractal Analysis; Contour Fluctuations; Biomineralization Process; Otoliths; Diffusion-Limited Aggregation; Microscopic Aggregation Model.

Resumo

Nas últimas décadas, análise multifractal tem sido aplicado com sucesso para caracterizar a complexa organização temporal e espacial de diversos fenômenos naturais, como a dinâmica de batimentos cardíacos, a forma dendrítica de neurônios, vasos da retina, fraturas de rochas, etc. No entanto, os métodos comuns de análise multifractal aparentam não ser apropriados para a análise de estruturas quasi-unidimensionais, com complexidades muito longe de preencher um espaço bi-dimensional, porém mais complexas do que uma linha, tal como o contorno de objectos. Por esta razão, a caracterização das propriedades multifractais de contornos fechados até o presente momento tem permanecido insuficiente. Na presente tese, uma nova técnica, robusta, "The Traveling Observer" Multifractal Detrended Fluctuation Analysis, é apresentada. Esta nova metodologia representa a ponte entre os métodos utilizados para fractais geométricos e os utilizados para séries temporais, reduzindo as limitações das técnicas atualmente utilizadas para análise multifractal de contornos. Primeiramente, o contorno é mapeado numa série temporal de distâncias ao caminho central, definido pela harmônica de termo zero, tal como um observador virtual viajando ao logo deste caminho a uma velocidade constante. As flutuações ao longo do perímetro deste caminho central são registradas como uma série temporal ou angular, e o "The Traveling Observer" MF-DFA é então implementado para quantificar as correlações temporais desta série. A relevância de se estudar as propriedades fractais das flutuações de contorno é demonstrada através de várias aplicações para dados naturais e simulados, destacando as vantagens dessa nova abordagem. Os resultados indicam que o novo processo pode capturar as características intrínsecas do processo de crescimento, oculto nas flutuações de contorno, e que são refletidas nos parâmetros multifractais. De fato, estes parâmetros podem ser utilizados como descritores de forma em problemas de classificação. Por outro lado, suas interpretações vão além da simples classificação de forma, expondo características significativas e por vezes inesperadas sobre as estruturas naturais e seu crescimento.

Palavras-chaves: Análise Multifractal; Flutuações do Contorno; Processo de Biomineralização; Otólitos; Agregação por Difusão Limitada; Modelo de Agregação Estocástico Microscópico.

Samenvatting

In de afgelopen decennia is multifractale analyse met succes toegepast op de complexe temporele en ruimtelijke organisatie van diverse natuurlijke fenomenen zoals hartslagdynamiek, de dendritische vorm van neuronen, retinale vaten, rotsbreuken, etc. Echter, gangbare methoden voor multifractal analysis lijken niet gepast voor het analysen van quasi-ééndimensionale structuren die veel minder complex zij dan 2D-vullende structuren, maar toch complexer dan een lijn; bijvoorbeeld de contouren van objecten. Daarom bleef de karakterisering van multifractale eigenschappen van gesloten contouren tot heden tamelijk ongrijpbaar. Hier wordt een nieuwe, robuuste, techniek, "The Traveling Observer" Multifractal Detrended Fluctuation Analysis gepresenteerd, welke de kloof tussen de methoden die worden gebruikt voor geometrische fractals en deze die gebruikt worden voor tijdelijke serie overbrugt. Dit vermindert de beperkingen op de bestaande multifractale technieken contouren an te analyseren. De procedure beeldt eerst de contour of op een "tijdreeks" van afstanden van het centrale pad (gedefinieerd door harmonische term nul), zoals waargenomen door een virtuele waarnemer die langs deze weg bij constante hoeksnelheid beweegt. De schommelingen van het centrale pad van de contour omtrek zijn geregistreerd als een " tijdreeks," en de MF-DFA wordt vervolgens geïmplementeerd om de " tijdelijke" correlaties van deze serie te kwantificeren. De relevantie van het bestuderen van de fractale eigenschappen van de contourfluctuaties wordt gedemonstreerd door verschillende toepassingen van natuurlijke en gesimuleerde data, met aandacht voor de voordelen van deze nieuwe aanpak. De resultaten geven aan dat de nieuwe procedure intrinsieke kenmerken van het groeiproces, verborgen in de contourfluctuaties, kan beschrijven die gereflecteerd worden door de multifractale parameters. In feite kunnen deze parameters worden gebruikt als vormbeschrijvingen in classificatieproblemen, in analogie met andere traditionele kwantitatieve methoden voor vormanalyse. Aan de andere kant goat hun interpretatie verder dan eenvoudige vormclassificatie, met als genolg het blootleggen van zinvolle en soms onverwachte eigenchappen van natuurlijke structuren en hun groei. Zo heeft men bijnabeeld net verband tussen multifractale kenmerken van otoliet-contourschommelingen en grootte van een vis en de leeftijd van maturiteit geobserveerd, en de eigenschappen van aggregaten gegenereerd door middel van een rekenmodel op verschillende groeiomstandigheden wijken nauwe correspondentie met thermodynamische gedrag van magnetische modelsys-

temen te vertonen.

List of Figures

List of Tables

Table of Contents

1   Introduction

The understanding of the behavior of simple natural systems such as molecular structures, complex phenomena such as earthquakes, and the underlying stochastic processes, has been the object of study of numerous researchers from different fields of science, including Oceanography, Biology, Geology, and, mainly, Physics, over the last century. Scaling and fractal geometry represent concepts of statistical physics introduced roughly four decades ago, which brought about a breakthrough in improving the understanding of diverse phenomena. These two concepts, based on power laws, permitted the study of macroscopic patterns through the knowledge of microscopic components, and making connections between phenomena of different length scales (MEAKIN, 1998).

Benoit Mandelbrot coined the name of fractal geometry in 1975 (MANDELBROT, 1975) to describe geometrical patterns in nature, extrapolating the classical Euclidean approach, and since that time this geometry has assisted to describe a long list of natural structures, from microscopic aggregates to the clusters of galaxies. Before Mandelbrot, others researchers started to study fractal objects, such as Karl Weierstrass, who in 1872 considered functions that were everywhere continuous but nowhere differentiable, and Helge von Koch, who in 1904 discussed geometric shapes such as the Koch Snowflake. However, the visualization of the complex fractal objects, characterized by intricate-looking set of curves, was only possible with the advent of computers (PICKOVER, 2009).

The most notable concept related with a fractal is self-similarity of an object in terms of its geometrical appearance, i.e. parts of a fractal object look similar to the whole. For instance, deterministic fractals, as the Koch snowflake shown in Figure 1, can be conceptu-

ally described through this concept. However, fractals are indeed not limited to geometrical patterns. In the definition proposed by Mandelbrot in 1986: "*A fractal is a shape made of parts similar to the whole in some way*", one can interpret the word "shape" as any measure (concentration, eletric potential, probability, etc.) of a structure or a process, measured statically or dynamically, and the self-similarity can be found in various degrees (VICSEK, 1989).
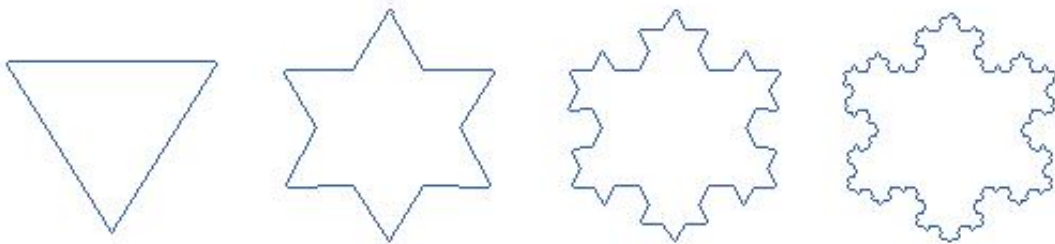
Figure 1: Illustration of three iterations of the Koch snowflake. The construction follows a recursive procedure, starting with an equilateral triangle: divide each line segment into three segments of equal length; draw equilateral triangles that have the central segments from the previous step as their bases; remove the line segments that represent the bases of the triangle drawn in the previous step.

For instance, only deterministic or mathematical fractals demonstrate exact self-similarity. In the case of random fractals, which are the most common in nature, self-similarity is interpreted in statistical sense (VICSEK, 1989; MEAKIN, 1998), i.e. the statistical measures of a phenomenon are invariant to the change of the length scale on which measurement is performed. For both deterministic and stochastic self-similarity, fractal geometry transforms complex irregularities that look similar under different resolutions, as shown in Figure 2, that could represent an additional source of complexity for some classical approaches, into a source of simplicity (SEURONT, 2010).

The principal feature of a fractal is that the relationship between the measure of a certain feature N of this phenomenon on scale of measurement (or length, or time) ϵ follows a power law

$$N\left(\epsilon\right) \sim \epsilon^{-D}. \tag{1.1}$$

The scale exponent D is the fractal dimension calculated as $D = lim_{\epsilon \to 0} \left[\frac{log(N)}{log(\epsilon)}\right]$, in prac-
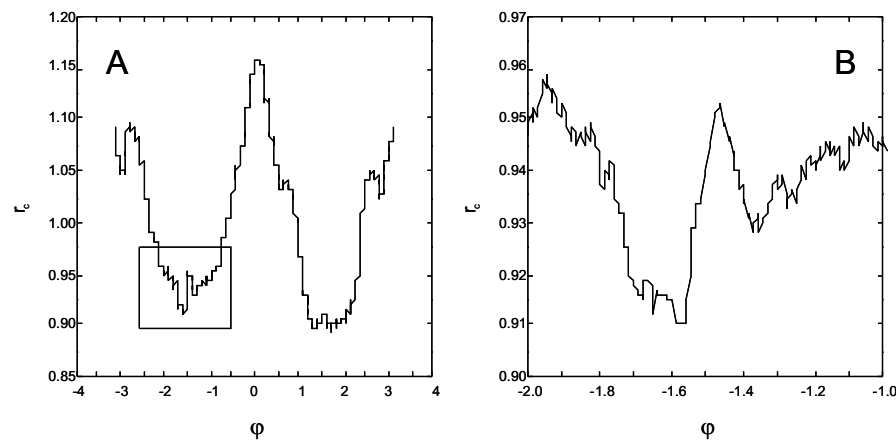
Figure 2: Contour fluctuations of a fish otolith at different angles. It is seen that just by looking at the two structures, one cannot determine which is local, and which is global.

tice obtained as the slope of the regression line of the scatterplot of $log(N)$ versus $log(\epsilon)$ (FEDER, 1988). Hence, one of reasons for the success of fractal theory in many scientific fields starts from its capability to explain complex systems using a relatively low number of parameters, the fractal dimensions.

Among the diverse fields of fractal applications, far-from-equilibrium growth phenomena have great importance, being commonly observed in many fields of science and technology, such as viscous fingering (fluid-fluid interaction; Fig. 3A), crystal growth (Fig. 4) and electrodeposition of ions onto an electrode (Fig. 5A). The far-from-equilibrium growth is characterized by presence of a continuous and sufficiently strong force that pushes it far from its natural state of rest; by the evaluation of the properties of this process, such as phase transitions and critical exponents; and by the possibility to find new phenomena that arise from the imposed conditions. Furthermore, due to instability of the system, it is easier to control a larger variety of patterns and assembling structures than in near-equilibrium state (COMMITTEE ON CMMP 2010, SOLID STATE SCIENCES COMMITTEE, NATIONAL RESEARCH COUNCIL, 2007).

Microscopic fractal growth models such as Diffusion Limited Aggregation - DLA, Eden model or Ballistic Aggregation, are often used to describe this kind of phenomena. For instance, objects on Figures 3A and 5A are similar to a DLA cluster shown in Figure 5B. These growing fractals are scale-invariant objects, and the theories and methods developed
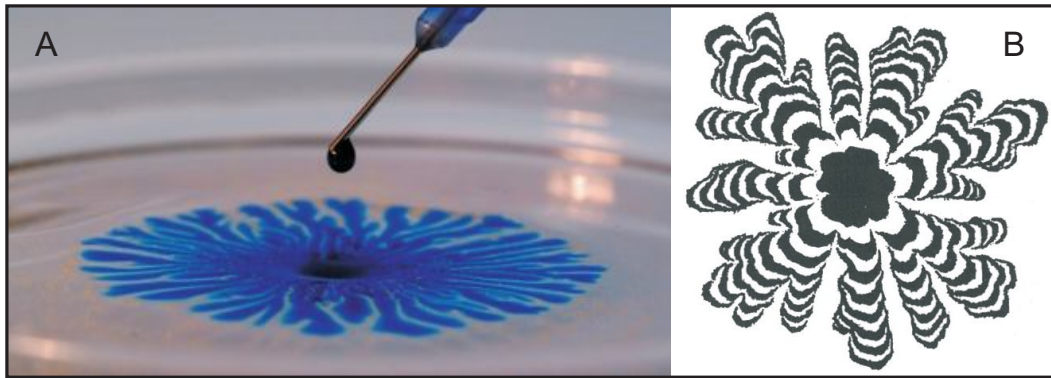
Figure 3: (A) Illustration of viscous flow (fluid-fluid interaction), similar to the results (B) obtained by Meakin et al. (1987) on the simulations of a off-lattice diffusion aggregation model.

to study far-from-equilibrium growth phenomena also contemplate scale invariance, therefore, these two theories brougth about a significant advance in the investigation of growth processes, including scaling behavior (VICSEK, 1989).
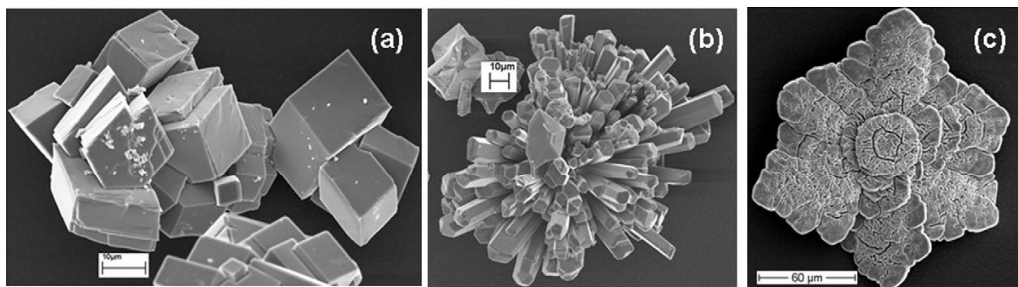
Figure 4: The crystalline polymorphs of calcium carbonate: (a) calcite, (b) aragonite, (c) vaterite (MUKKAMALA; ANSON; POWELL, 2006)
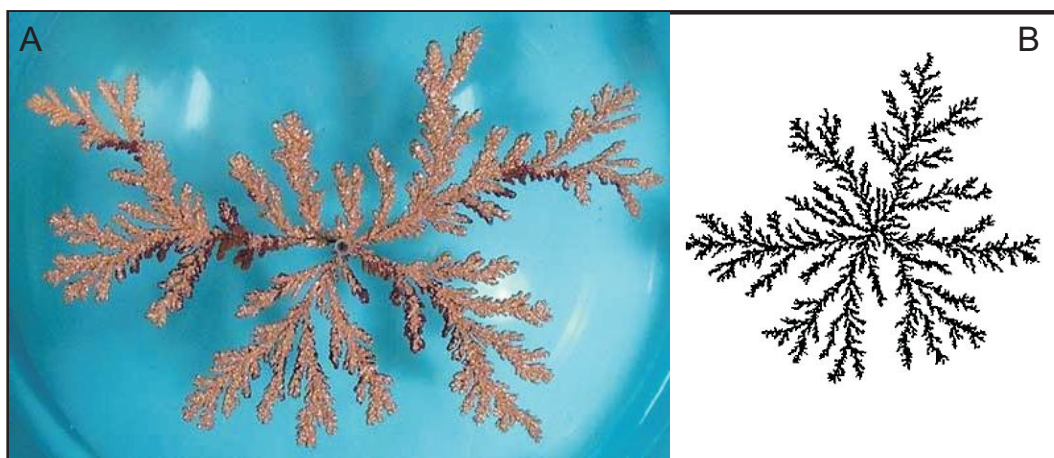
Figure 5: (A) Copper aggregate formed from a copper sulfate solution in an electrode position cell (JOHNSON, 2006); (B) off-lattice DLA cluster with 5×10^5 particles aggregated (BARABÁSI; STANLEY, 1995)

Many phenomena in nature are investigated using fractal analysis present interwoven components with different fractal properties. Due to this complexity of behavior, another concept in fractal analysis appears to better describe these types of phenomena: multifractality. The unique scale exponent, obtained in the monofractal theory, is adequate for describing a uniform set (uniform distribution of a measure). For more complex sets that exhibit a hierarchy of scaling exponents at different scales, application of monofractal analysis yields an "average" (or effective) fractal dimension and a generalized multifractal approach provides a more adequate description.

More precisely, consider mass probability $p_i(\epsilon)$ for each region of size (scale) ϵ and the partition function $Z_q(\epsilon)$ defined by

$$Z_q(\epsilon) = \sum_i p_i(\epsilon)^q. \tag{1.2}$$

Using this partition function one can describe the structure at different scales, that is, if one considers the qth generalized moment for large positive q, then $Z_q(\epsilon)$ will be dominated by those parts of the structure with largest values of $p_i(\epsilon)$, while for q negatively large $Z_q(\epsilon)$ is dominated by parts of the structure with smallest (non-zero) values of $p_i(\epsilon)$ (CHHABRA; JENSEN, 1989; MEAKIN, 1998). Thus, parameter q serves as a "magnification glass", and it can assume values between $-\infty$ and $+\infty$, but in practical applications it is truncated at some large positive and negative values. In this way, multifractal analysis captures the inner variation in a system by resolving local densities and expressing them by a hierarchy of exponents, rather than a single fractal dimension (FEDER, 1988; MEAKIN, 1998).

In recent decades multifractal analysis has been successfully applied to characterize the complex temporal and spatial organization of such diverse natural phenomena as heartbeat dynamics (IVANOV et al., 1999), the dendritic shape of neurons (FERNÁNDEZ et al., 1999), retinal vessels (STOSIC; STOSIC, 2006), rock fractures (XIE; WANG; KWAśNIEWSKI, 1999), and intricately shaped volcanic ash particles (DELLINO; LIOTINO, 2002). In what follows, some of the most common techniques applied to determine the multifractal properties of geometric objects and temporal series are briefly described.

Geometrical multifractals represent a special case when the measure of interest is homogeneously distributed over the observed structure. Growing structures, as the Diffusion Limited Aggregation (DLA), widely used to model far-from equilibrium phenomena, are good examples of this kind of multifractals and their fractal properties are frequently measured by the amount of mass M_0 within a box of linear size L (TéL; VICSEK, 1987).

Considering the mass distribution observed for different grids of size ℓ, such that $a << \ell << L$ (where a is the lattice constant and L is the linear dimension of the system), the generalized dimension D_q can be defined as (TéL; FÜLÖP; VICSEK, 1989)

$$\sum_i \left(\frac{M_i}{M_0}\right)^q \sim \left(\frac{\ell}{L}\right)^{(q-1)D_q} \tag{1.3}$$

where M_0 is the total mass, and M_i is the mass (number of pixels) within the ith box. The generalized dimensions D_0, D_1, and D_2 correspond to the capacity (or box-counting) dimension, information (or Shannon) dimension, and correlation dimension, respectively. Finally, $D_{-\infty}$ and $D_{+\infty}$ represent the limits of the generalized dimension spectrum, where the measure of interest is "most dilute" and "most dense", respectively. For monofractals, all the generalized dimensions coincide, being equal to the unique fractal dimension, i.e. the fractal dimension is independent of q.

As mentioned before, multifractal analysis expresses the variation in a system by a hierarchy of exponents, the so called $f(\alpha)$ spectrum, achieved through the Legendre transform

$$f\left[\alpha\left(q,\ell\right)\right] = q\alpha\left(q\right) - \tau\left(q\right), \tag{1.4}$$

where

$$\alpha\left(q\right) = \frac{d\tau(q)}{dq} \tag{1.5}$$

and $\tau(q)$ is the mass correlation exponent of the qth generalized moment, defined as $\tau(q) = (q-1)D(q)$. The singularity spectrum provides a mathematically precise and naturally intuitive description of the multifractal measure in terms of interwoven sets (regions) with singularity strength α (see e.g. Chhabra and Jensen, 1989, for more details). In the case of geometrical multifractals, $f(\alpha)$ may be understood as the fractal dimension of these sets.

For a monofractal structure, the singularity spectrum produces a single point in the $f(\alpha)$ plane, whereas multifractal objects yield a single humped function.

Perhaps the most popular method used to capture fractal and multifractal properties of geometrical objects is the box counting method, defined by Russel et al. (1980). This method consists in covering the object with a grid of N_0 boxes of size ℓ (Fig. 6) and determining the number of non-empty boxes N_t. The fractal dimension is then determined from the Equation 1.1, where the scale ϵ is equal to ℓ/L.

To investigate the object over a range of generalized moments, the generalized dimensions for each q can be obtained from

$$D_q(\epsilon) = \frac{ln\left[\sum (N_t/N_0)^q\right]}{ln(\epsilon)} \cdot \frac{1}{(q-1)}. \tag{1.6}$$
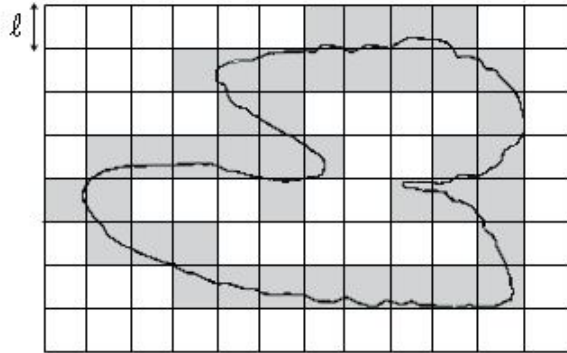
Figure 6: Example of a set of boxes with size ℓ to determine the fractal dimension through the box-counting method

Another widely used method for geometrical fractals is the sand box. In this method, the main quantity is the mass $M(R)$ (the number of particles) within a region of radius R centered typically on the fractal origin. The relation of these two measures also follows the power law described in Equation 1.1. in the form $M(R) \sim R^{D_0}$, from witch the fractal dimension is obtained. However, according to Tél et al. (1989), for some geometrical multifractals, this power law exists, but the generalized dimension D is equal to $D_{-\infty}$ instead of D_0 if the centre is the origin of the fractal. Furthermore, the singularity strength α and the

function $lnM(R)$ versus lnR will be dependent of the choice of the sand box center.

To minimize this problem, the former authors introduced the generalized sand box method, that uses the average value of the masses $M(R)$ and their powers over randomly distributed centres on the fractal. Based on this modification, the equivalent of Equation 1.3 for this method becomes

$$\left\langle \left(\frac{M(R)}{M_0} \right)^{q-1} \right\rangle \sim \left(\frac{R}{L} \right)^{(q-1)D_q} \tag{1.7}$$

These two techniques are adequate to describe fractals in a two dimensional plane. Other multifractal techniques are frequently used to describe multifractality of one dimensional data measured in homogeneous time intervals, developed to analyze complex systems that frequently exhibit noisy and non-stationary time series (MUZY; BACRY; ARNEODO, 1991; MURGUíA; URíAS, 2001; KANTELHARDT et al., 2002; KANTELHARDT, 2009), that represents a difficult task for classical statistical tools (MéNARD et al., 2006). In fact, the non-stationary behavior of complex systems can hide trends and heteroskedasticity that could lead to a spurious detection of correlations. However, the multifractal techniques developed in the last decade can avoid this problem by removing the trends and concentrate on the analysis of the fluctuations (OSWIECIMKA; KWAPIEN; DROZDZ, 2006). They often uncover scaling laws that characterize the studied phenomena through fractal (or multifractal) scaling exponents, which can be used in comparison with other systems and with models, modelling the time series, predictions regarding extreme events or future behavior and characterization of the system phase transitions (KANTELHARDT, 2009).

Muzzy et al. (1991) have proposed a robust multifractal analysis based on the wavelet transform (WT) that can be applied to determine the singularity spectrum of any experimental signal. In the wavelet transform modulus maxima (WTMM) method, the partition function of Equation 1.2 is constructed using the capability to detect all the singularities of a large class of signals through the local maxima of the WT, $|T_g(\epsilon, x)|$, at a given scale $\epsilon > 0$, and arranging them in an hierarchical order (MUZY; BACRY; ARNEODO, 1991). More precisely, instead of boxes, this method covers the entire support with wavelets of different sizes.

The WT for a specific wavelet function g of a signal $s(x)$ is defined as

$$T_g(\epsilon, x_0) = \frac{1}{\epsilon} \int_{-\infty}^{+\infty} s(x) \bar{g}\left(\frac{x - x_0}{\epsilon}\right) dx \tag{1.8}$$

and the partition function becomes

$$Z(\epsilon, q) = \sum_{\{x_i(\epsilon)\}_i} |T_g(\epsilon, x(\epsilon)|^q \approx \epsilon^{\tau(q)} \tag{1.9}$$

Then, the singularity spectrum can be determined from the Legendre transform in Equation 1.4 of the partition function scaling exponent $\tau(q)$

Another important technique used for time series, as efficient as the WTMM method, however requiring a lesser computational effort (KANTELHARDT et al., 2002), is the Multifractal Detrendeded Fluctuation Analysis (MF-DFA). It is a generalization of the so called Detrended Fluctuation Analysis, DFA (PENG; BULDYREV; HAVLIN, 1994), widely-used technique for the determination of monofractal scaling properties and the detection of long-range correlations in noisy, nonstationary time series. In the case when the series presents different scale exponents, the use of MF-DFA is preferable.

Although the methods described above are well established in the scientific community, they do not seem appropriate for analyzing quasi-one-dimensional structures, with complexity far from filling two dimensional space, but more complex than a line. For instance, the contour represents an important feature extracted from natural and artificial objects and, in many cases, displays this characteristic. The contour of objects has been intensively studied in a wide range of scientific fields, since all objects present a closed or an opened contour. Furthermore, from a two dimensional point of view, the contour represents the surface of a natural structure that is in direct contact with the environment, and its study can reveal important results in this respect. Nevertheless, the characterization of multifractal properties of closed contours has up to date remained rather evasive.

Motivated to reduce the limitations present in existing multifractal techniques to analyze contours, and in order to demonstrate the relevance of studying the fractal properties of this important feature, we introduce here a new, robust, technique, "The Traveling Observer"

Multifractal Detrended Fluctuation Analysis, which bridges the gap between the methods used for geometrical fractals and those used for temporal series. In the next chapter we describe the details of this procedure, highlighting the problems observed in the classical methods, and the advantages of this new approach.

The following chapters show some applications of the "Traveling Observer" MF-DFA and demonstrate the capability of the multifractal analysis of the contour fluctuations to reveal meaningful and sometimes unexpected information about natural structures and their growth processes. In chapters 3 and 4, contour fluctuations of fish otoliths are analyzed. First, the multifractal behavior of otoliths during the fish life was investigated, and then the existence of different patterns of multifractality among fish species, and the capability of the multifractal parameters to classify otoliths of different species were evaluated. Finally, in chapter 5, a microscopic aggregation growth process under different growing condition is analyzed, considering both the morphological changes in the aggregates and the multifractality of their perimeter fluctuations.

2 The "Traveling Observer" Multifractal Detrended Fluctuation Analysis

2.1 Introduction

When we use our vision capability, we often try to identify some characteristics of an object to learn about it or to recognize it among another objects. Some of these characteristics could be color, texture, size and the nature of the border or contour (Fig. 7). The latter is often used to describe properties of boundaries in surface interaction, shapes and roughness of objects. Artificial objects usually present regular and smooth shapes, that are easily described by the traditional Euclidean geometry. However, natural structures usually reveal far more complex patterns. The boundaries that form natural surfaces and contours are often not smooth. Natural forms (landscapes, mountain, coastlines, trees, vegetation cover) are irregular and rough in appearance.

The classical view of object structure considers roughness as a surface phenomenon that does not penetrate into the form that constitutes the object per se. The objects of classical analysis are composed of compact differentiable manifolds, smooth curves or surfaces that include their boundaries. In this view, natural contours consist of a superficial coating of texture or irregularity that is attached to a compact underlying structure. Hence, rough contours can be decomposed into smooth differentiable trends and rough additions (GILDEN; SCHMUCKLER; CLAYTON, 1993). In the case of fractal theory, roughness is considered as the main feature evaluated, since it captures the complexity of the shape in terms of the level of
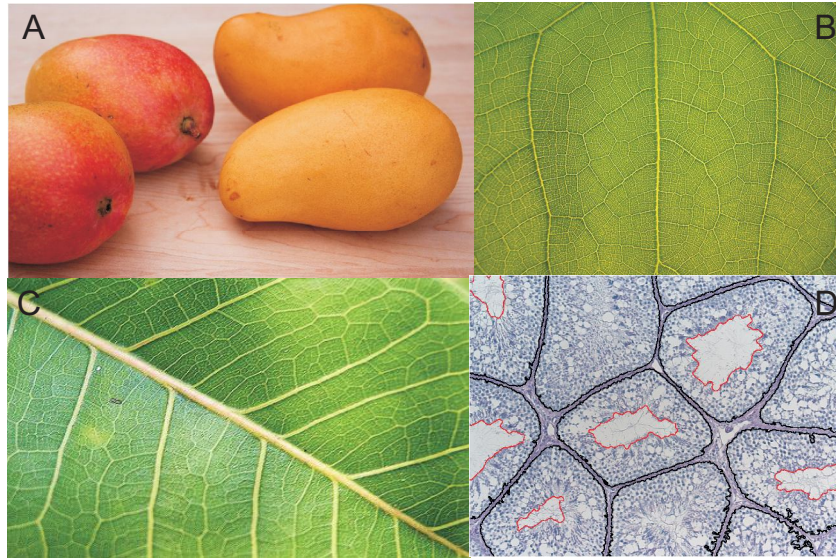
Figure 7: Ilustration of some characteristics that we visibly used to describe and distinguish objects. (A) Colors and size; (B) and (C) texture; and (D) borders and contours.

protrusions and cavities at different scales, rather than shape in the sense of morphometry. This characteristics is important because variations in the boundary of a natural structure during growth is a response to (i) external boundary conditions (surface interaction) and (ii) the internal mechanisms of the growth process. Therefore, the analyses of local and global fluctuations of the contour may provide useful information on both.

However, when we assume a contour shape as a monofractal, we get only a single scale exponent (fractal dimension), which often cannot adequately describe contour complexity. Thus a generalized multifractal approach is needed (HARTE, 2001). Practical difficulties have thus far prevented the full use of multifractal analysis to describe closed contours. Such traditional techniques have been demonstrated to be rather problematic because of the fact that boxes which contain a small (or zero) number of particles (or pixels) give an anomalously large contribution to the partition function, and consequently they do not yield reliable results for negative q (FERNÁNDEZ et al., 1999). Another problem is that the results turn out very sensitive to the choice of the box size range. Tél et al. (1989) proposed an alternative method (the "Generalized Sand Box Method") to solve the first problem, nevertheless the second issue still remains problematic. These methods also assume the contour is a geometrical fractal, and thus important fine fluctuations around the quasi-one-

dimensional structure of the contour perimeter may be ignored.

To overcome these technical problems, a new technique to investigate whether fluctuations of the contour can reveal more information than its bare morphological appearance is proposed here, combining Regular Fourier Analysis (RFA) and Multifractal-Detrended Fluctuation Analysis (MF-DFA). First, the contour is mapped onto a "time series" of distances from the central path, defined by harmonic term zero (Fig. 8) as observed by a virtual observer traveling along this path at constant angular speed. The fluctuations from the central path of the contour perimeter are registered as a "time series," and the MF-DFA is then implemented to quantify the "temporal" (sequential angular) correlations of this series.
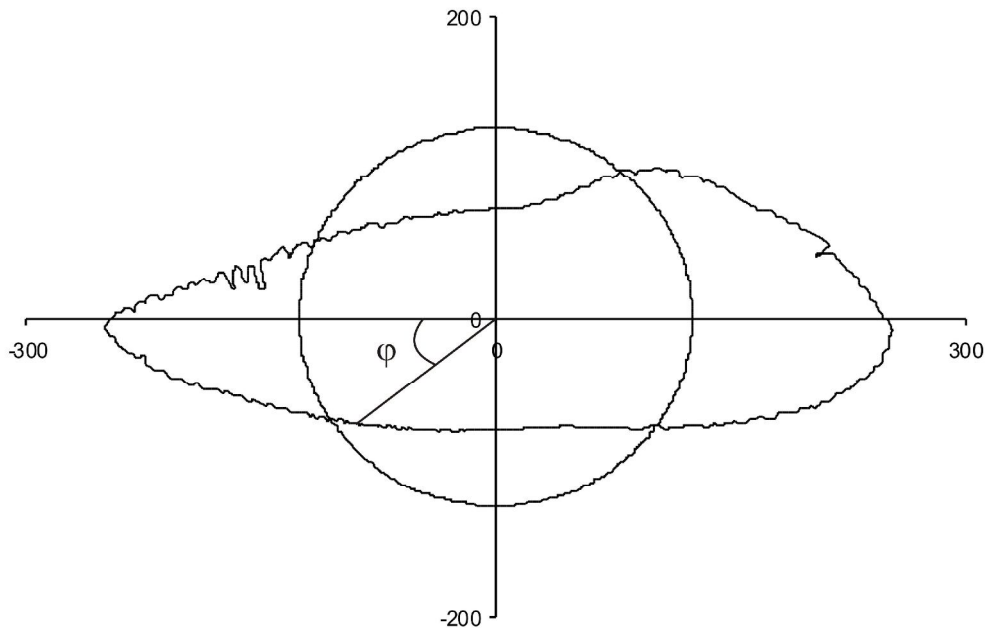
Figure 8: Schematic representation of the superposition of the standard circular shape (zero-th harmonic term) with a contour, used to define the periodic series of the contour fluctuations.

2.2 The Method

2.2.1 Data series construction

The data series is constructed using the values of the radius of the contour r at the angle φ, normalized by the zero-th harmonic (Fig. 8), with φ varying between $-\pi$ and π.

The normalized (dimensionless) contour radius r_c at point i of the contour $(i = 1, ..., k)$ is defined as

$$r_c(\varphi) = \frac{\sqrt{x_{(i,\varphi)}^2 + y_{(i,\varphi)}^2}}{a_0} \tag{2.1}$$

where x and y are the coordinates of the ith contour pixel at the angle φ, and a_0 is the coefficient of zero-th degree term, defined as the mean of the k radii observed in the structure, $a_0 = k^{-1} \sum_{i=0}^{k-1} r_i$ (LESTREL, 1997). The zero-th degree term represents the contribution of a circle centered on the center of mass of the structure. Therefore r_c is less than one if the contour point lies inside the circle, and it is greater than unity if the point lies outside the circle.

There are two advantages of using the RFA: (1) the multifractal analysis becomes invariant to size, since the zero-th degree term is proportional to the size of the image; (2) complex morphological contour may present multiple values for a single angle due to protrusions and cavities. The last feature is in fact commonly considered a limitation for the use of RFA, but it is precisely the opposite in the current approach, because this effect induces noise into the data series, and the multifractal characteristics become more pronounced. That is, at the same angle, the structure could present sites with high, moderate and low probability of aggregation (Fig. 9), that characterize the complexity of the structure analyzed.

The current mapping of the data may be considered as a time series of the values of the distance from the actual contour to the basic regular shape (defined by the zero-th harmonic), as seen by an observer traveling along the regular shape at constant angular speed. Using this time series the multifractal analysis based on the MF-DFA method proposed by Kantelhardt et al. (2002) to analyze multifractal properties of non-linear temporal series is carried out.
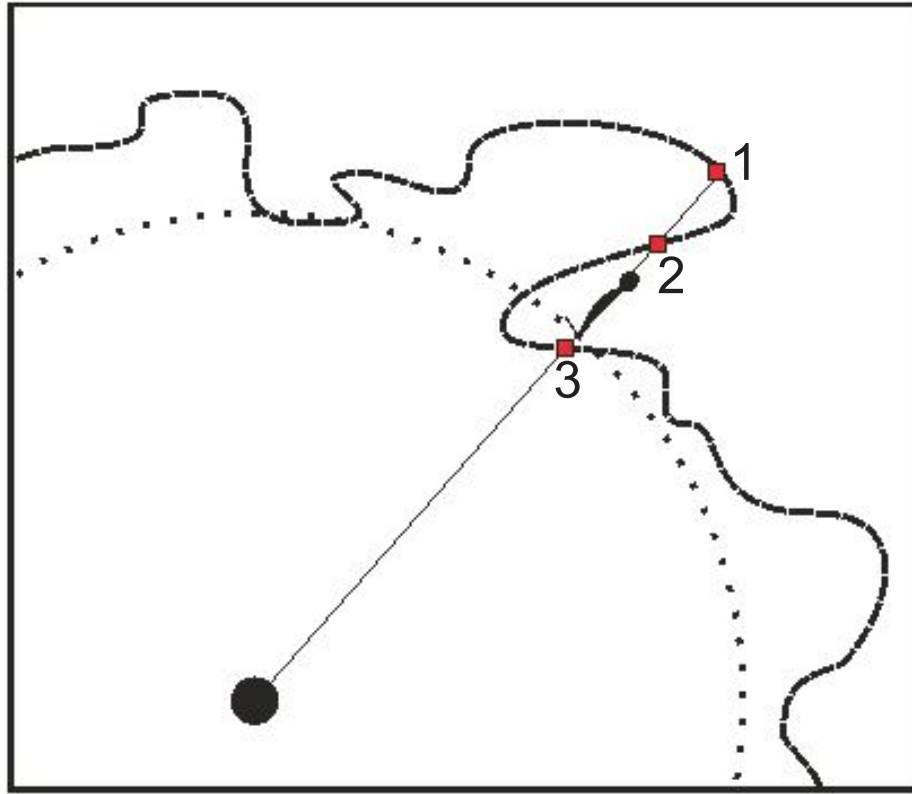
Figure 9: Schematic representation of the "traveling observer" procedure, illustrating a possible configuration of points visualized at some angle. Considering the "active zone" of the structures (the outer part of the surface that is exposed to aggregation), the point 1 has higher probability, point 2 has moderate and point 3 has low probability of aggregation.

2.2.2 Multifractal Detrended Fluctuation Analysis (MF-DFA)

Let x_k a periodic series of r_c values between $-\pi$ and π, of length N, corresponding to the number of pixels that form the contour, having mean $\overline{x}$.

(i) First an integrated series Y_i is calculated as

$$Y_i \equiv \sum_{j=1}^{i} (x_j - \overline{x}), i = 1, ..., N;$$

(2.2)

(ii) The integrated series Y_i is divided into $N_\ell \equiv [N/\ell]$ non-overlapping segments of equal length ℓ, where symbol $[.]$ stands for integer part.

(iii) For all of the N_ℓ segments the fluctuation function $F^2(\ell, \nu)$ is calculated as

$$F^2(\ell, \nu) = \frac{1}{\ell} \sum_{i=1}^{\ell} \{Y\left[(\nu-1)\ell+i\right] - y_\nu(i)\}^2, \nu = 1, ..., N_\ell, \tag{2.3}$$

where $y_\nu(i)$ is the fitting polynomial in segment ν, representing the local trend.

(iv) The fluctuation function of qth degree for segment size ℓ is given by

$$F_q(\ell) = \left\{ \frac{1}{N_\ell} \sum_{\nu=1}^{N_\ell} \left[F^2(\ell, \nu)\right]^{q/2} \right\}^{1/q} \tag{2.4}$$

where q can assume any real value between $-\infty$ and $+\infty$ except zero, but in practical applications it is truncated at some large positive and negative values.

(v) The function $F_q(\ell)$ represents the partition function for this case (as previously introduced by Eq. 1.2) and follows a power law

$$F_q(\ell) \sim \ell^{h(q)}, \tag{2.5}$$

where the generalized exponent $h(q)$ is the slope of the linear regression between $log(\ell)$ and $log(F_q(\ell))$. For a monofractal process $h(q)$ is constant (independent of q), and for a multifractal process $h(q)$ is a decreasing function of q.

As is common in the literature using the MF-DFA approach, besides the functional form $h(q)$, the multifractal properties of contours are also investigated based on the so called singularity spectrum $f(\alpha)$, achieved through the Legendre transform

$$f\left[\alpha\left(q, \ell\right)\right] = q\alpha\left(q\right) - \tau\left(q\right), \tag{2.6}$$

where

$$\alpha\left(q\right) = \frac{d\tau(q)}{dq} \tag{2.7}$$

and $\tau(q)$ is the mass correlation exponent of the qth moment, defined as $\tau(q) = qh(q) - 1$. The singularity spectrum provides a mathematically precise and naturally intuitive description of the multifractal measure in terms of interwoven sets with singularity strength α, whose Hausdorff dimension is $f(\alpha)$ (see e.g. Chhabra and Jensen (1989) for more details). In the

case of a monofractal structure, the singularity spectrum produces a single point in the $f(\alpha)$ plane, whereas multifractal objects yield a single humped function.

A set of parameters can be extracted from the multifractal spectra (Fig. 10) for characterizing contour complexity, each with a clear intuitive interpretation:

a) α_0, position of the maximum of $f(\alpha)$, corresponding to the point where $q \to 0$.

b) $\Delta\alpha$, the width of the spectrum, estimate of the range of α where $f(\alpha) > 0$, obtained as $\Delta\alpha = \alpha_{max} - \alpha_{min}$.

c) $\Delta\alpha+$, the contribution of the positive part of q in the range of the spectrum, estimated by $\Delta\alpha+ = \alpha_0 - \alpha_{min}$.

d) $\Delta\alpha-$, the contribution of the negative part of q in the spectrum range, estimated by $\Delta\alpha- = \alpha_{max} - \alpha_0$.

These four parameters serve to describe the multifractality of the signal, and hence the "complexity"of the contour shape. If α_0 is high, the signal is correlated and the underlying process "loses fine structure"(exhibits a smoother contour). The width $\Delta\alpha$ measures the range of fractal exponents in the signal; therefore, the wider the range, the "richer"are the multifractal characteristics of the signal. Parameters $\Delta\alpha+$ and $\Delta\alpha-$ work as a measure of the dominance of low and high fractal exponents, respectively. The larger $\Delta\alpha-$ the stronger the weight of high fractal exponents (corresponding to fine structure), and more smooth-looking the spectra if $\Delta\alpha+$ dominates.

Two different types of multifractality in time series can be distinguished, both requiring a multitude of scaling exponents for small and large scale fluctuations: a) multifractality of a time series can be due to a broad probability density function for the values of the time series; and b) multifractality can also be due to different long-range correlations for small and large fluctuations (KANTELHARDT et al., 2002). Following these authors, the type of multifractality of contours is determined by analyzing the corresponding randomly shuffled series. The shuffled series from multifractals of type b) exhibits simple random behavior, $h(q) = 0.5$
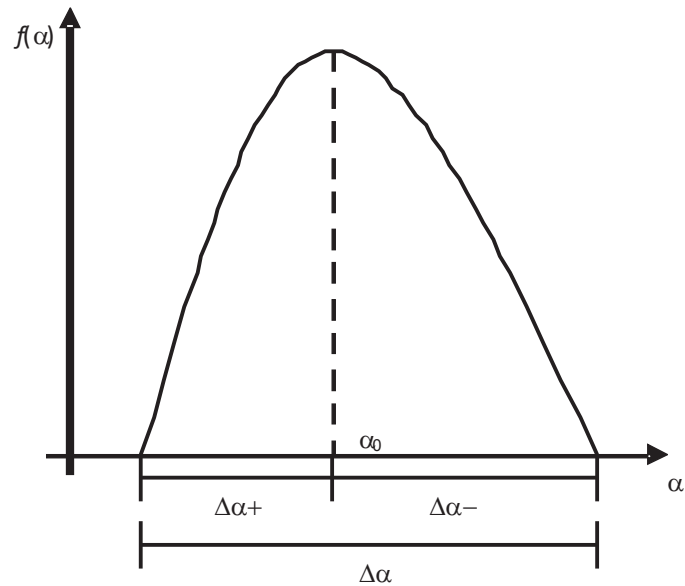
Figure 10: Schematic representation of the multifractal parameters extracted from the singularity spectrum.

(non-multifractal scaling), while for multifractals of type a) the original $h(q)$ dependence is not changed (since the multifractality is due to the probability density, which is not affected by the shuffling procedure). If both kinds of multifractality are present in a given series, the shuffled series demonstrates weaker multifractality than the original one.

A dedicated program was written in the C programming language to implement numerically the described methodological procedure. The software (calcradius ver. 1.1) was developed with a user friendly interface, and is available for download from the link http://www.pgbiom. ufrpe.br/downloads/calcradius/.

3 Fish First Sexual Maturity Uncovered by Multifractal Analysis of Saggital Otolith Contour Fluctuations

3.1 Introduction

To demonstrate the power of the proposed novel procedure, we apply it to sagittal oto-liths of two fish species, *Mugil curema* (Fig. 11A) and *Merluccius merluccius* (Fig. 11B). Otoliths are calcified concretions found in a fish's inner ear (Fig. 12) and are associated with the functions of hearing, balance, and orientation (SÖLLNER et al., 2003). They represent the "black-box" of teleost fishes (LECOMTE-FINIGER, 1999), i.e. an important source of informa-tion for ecological and biological knowledge of diverse fish species, as their physical and chemical composition can be used to draw conclusions of diverse nature, such as habitat, characteristics of daily, seasonal or annual growth, or stock structure and age (GREEN et al., 2009). The richness of this information source has become indispensable for the current stock evaluation and management practice (GREEN et al., 2009).

Inside of the fish inner ear, the otolith, sagitta, lapillus and asteriscus, are contained in optic sacs, sacculus, utriculus and lagena, respectively (Fig. 12A). These structures act as electro-mechanic sound and displacement transducers, converting the shear forces into electrical impulses by kinocilia deformation on the macula (sensory tissue) (POPPER; HOX-TER, 1981). The information is stored in the otolith during its biomineralization process, which starts at the otolith primordium (LECOMTE-FINIGER, 1999) and continues with the pre-
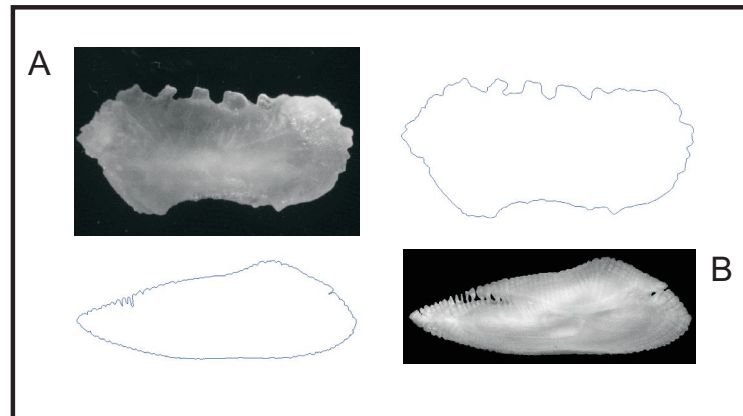
Figure 11: Examples of sagittal otoliths and their contours of (A) *Mugil curema* and (B) *Merluccius merluccius*

cipitation of calcium carbonate regulated by the endogenous rhythm of calcium metabolism (MUGIYA, 1987) and by secretion of neuropeptide in the inner ear (GAULDIE; NELSON, 1988). They consist of calcium carbonate crystals contained in a protein matrix (proteins represent 0.2 to 10% of otolith composition) (LECOMTE-FINIGER, 1999). This protein matrix is functionally essential in the process of otolith biomineralization, controlling the successive stages of biomineral creation and their resulting shapes (ALLEMAND et al., 2007). The precipitation of calcium carbonate is governed by the reaction (JOLIVIET, 2009)

$$Ca^{2+} + CO_3^{2-} \rightarrow CaCO_3 + H^+,$$
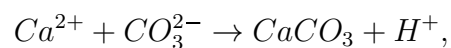
characterized by the saturation coefficient $Sa^2 = \lfloor Ca^{2+} \rfloor \lfloor HCO_3^{3-} \rfloor / K_s$, where K_s is the solubility product. The precipitation occurs only when the saturation coefficient is greater than unity.

Over the fish's life, the rhythm of calcium aggregation changes, reflecting the growth pattern of the fish and such periodic events as photoperiod variation, spawning, and migration (CAMPANA, 1999). These changes are reflected in the formation of micro- and macro-structures around the primordium (Panella, 1971), the chemical composition, thickness, and periodicity of formation of which are correlated with historic events and with the age of the fish (CAMPANA, 1999). Therefore, it is expected that the fluctuations of the border of the otolith can also be an expression of external and internal conditions over the growth
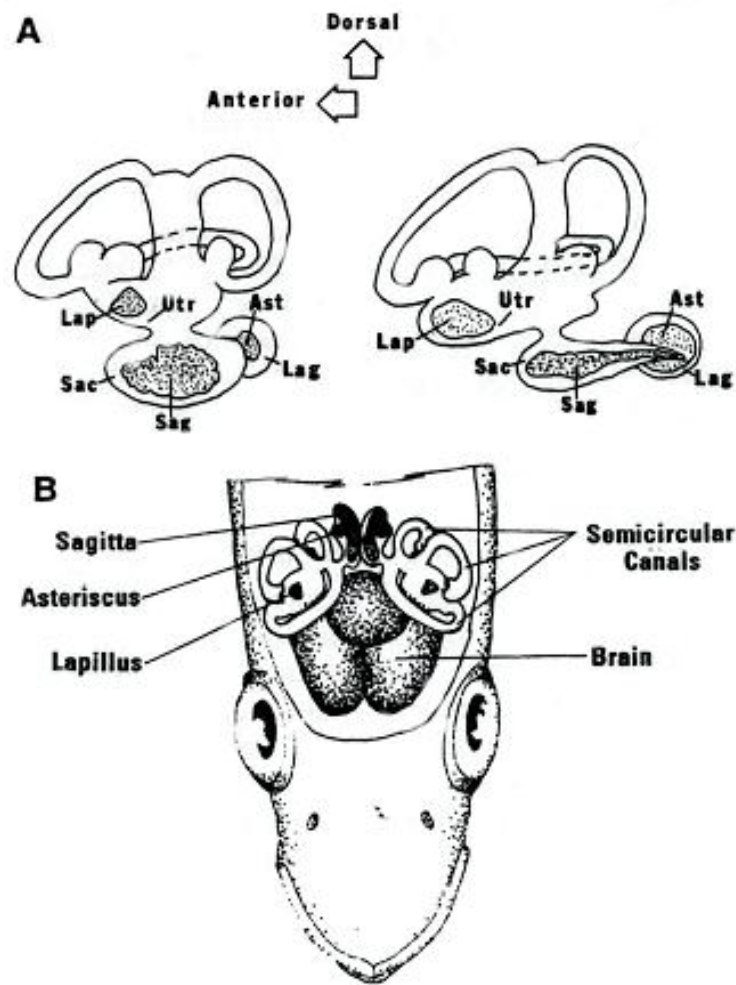
Figure 12: Anatomy of the inner ear. (A) Otoliths with the labyrinth system representation of the teleost fishes. (B) Dorsal view of the vestibular apparatus of a common teleost. Ast = asteriscus; Lag = lagenar vestibule; Lap = lapillus; Sac = sacular vestibule; Sag = sagitta; sc = semi-circular channels; utr = utricular vestibule.

process. Through the "traveling observer" MF-DFA (chapter 2), we find that a multifractal approach can discover relationships between contour features and such fish characteristics as size and age at maturity, previously accessible only through costly and cumbersome experimental techniques.

3.2 Image Sample

The sample was composed of 65 high-resolution otolith images of *Mugil curema*, from the north region of Pernambuco (Brazil), and 32 of *Merluccius merluccius*, from Port de La Selva (n = 13, Mediterranean Sea) and Galicia (n = 19, northeastern Atlantic Ocean). All *M.*

curema otolith images were obtained from the DIMAR lab (DEPAq/UFRPE) and they were captured using a charge-coupled device camera mounted on a microscope and processed using an image-analysis system developed for calcified structures (TNPC: Visilog software platform, NOESIS, France). *M. merluccius* otolith images were obtained from the image catalog of the project Anàlisi de FORmes d'Otòlits - AFORO (LOMBARTE et al., 2006). Otoliths were pre-processed to segment the otolith contours and were analyzed using the "traveling observer" MF-DFA. The data series was constructed using the radius of the otolith contour at an angle φ, normalized by the zero-th harmonic.

3.3 Results and Discussion

The multifractal analysis of otolith contours in two species reveals clear multifractal behavior. The generalized exponent $h(q)$, the slope of the linear regression between $log(\ell)$ and $log(F_q(\ell))$ (Fig. 13A), presents a monotonic decay with q (Fig. 13B), and the singularity spectrum has a humped shape (Fig. 13C). An observation of individual length and age provides solid proof that the multifractal properties of otolith contour reflects life history events. For *M. curema*, the α_0 distribution shows a peak at 23.9 cm (fork length) (Fig. 14a) and 3 years old (Fig. 14b). This peak closely corresponds to the length (23.3 cm) and age (2.8 years old) at first sexual maturity for both sexes, as documented previously by Santana *et al.* (2009) using gonads. Note that here we see no difference between the growth of males and females.

On the other hand, for *M. merluccius* plotting α_0 versus length/age (Fig. 15) reveals two different patterns. We attribute this behavior to the fact that this species has different growth rates between sexes, with females growing more quickly than males (MELLON-DUVAL et al., 2010; PIÑEIRO; SAÍNZA, 2003) and reaching maturity at different sizes and ages. The Mediterranean α_0 values show two peaks around 15.0 cm and 30.0 cm (total length) (Fig. 15a) and the corresponding peaks in age were one and two years old (Fig. 15b). A recent study of the reproductive pattern of *M. merluccius* from the Mediterranean Sea estimated
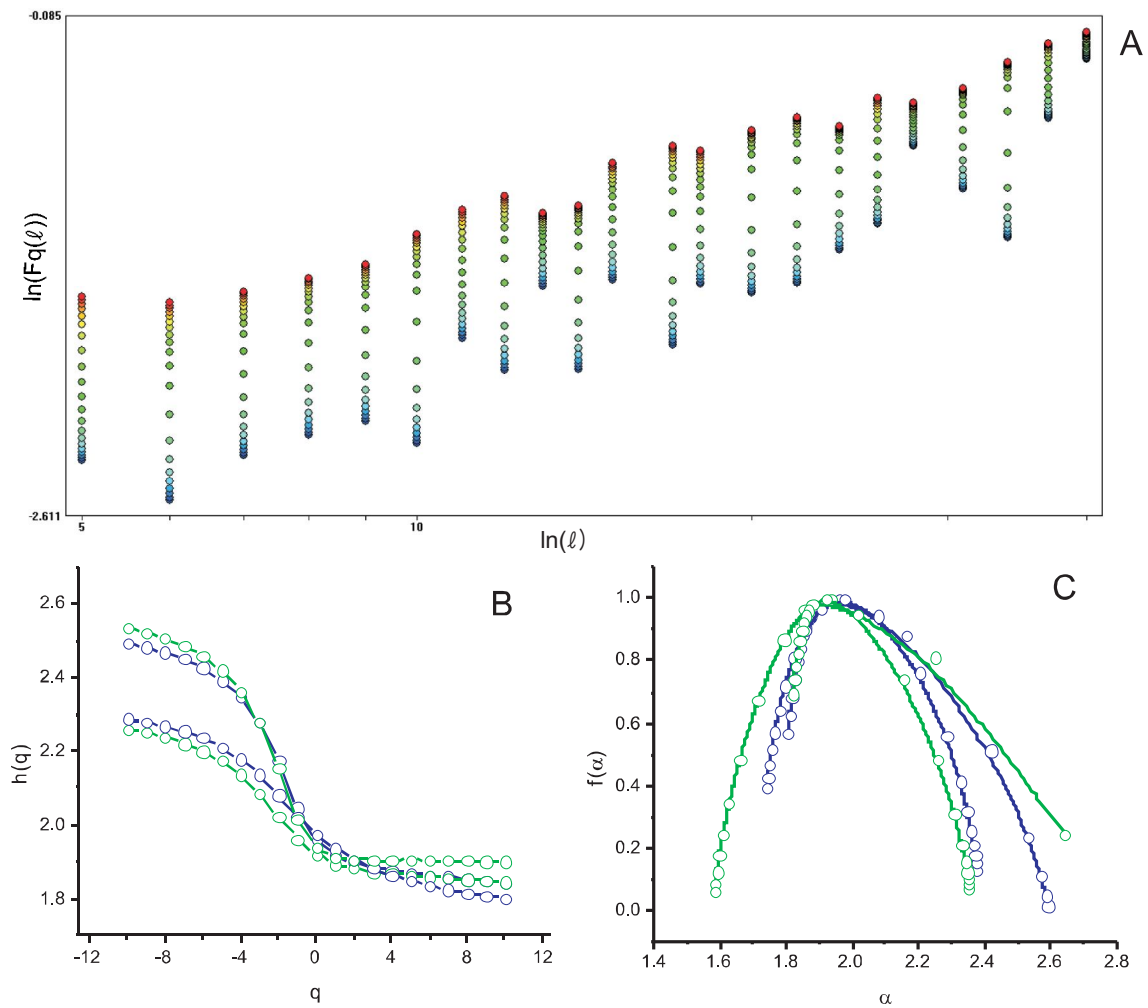
Figure 13: (A) Example of the log-log plot between the scale ℓ and the the partition function $F_q(\ell)$ obtained from the fluctuation contour of a *M. merluccius* otolith. (B) Plot of (a) the qth moment versus the generalized exponent $h(q)$ determined as the slope of the linear regression between $log(\ell)$ and $log[Fq(\ell)]$. (C) The singularity spectra $f(\alpha)$ derived from the fluctuation contour of two *M. merluccius* (blue) and two *M. curema* (green) otoliths.

the length at first maturity of females to be approximately 35.0 cm (RECASENS; CHIERICONI; BELCARI, 2008), which is very close to the second peak. Using the growth parameters determined by Mellon-Duval *et al.* (2009) for females, the corresponding age at first maturity is two years, precisely the age with the highest α_0 value in our analysis. The two maximum α_0 values for the Atlantic population were found to be 30.0 and 45.0 cm (total length) (Fig. 15c), which match well the lengths of first maturity estimated by Piñeiro and Saínza (2003) for males (32.8 cm) and females (45.0 cm) (Fig. 15d).

It is likely that there is less precision in the *M. merluccius* analysis due to the reduced number of individuals in the available dataset. Nevertheless, it is clear that changes in
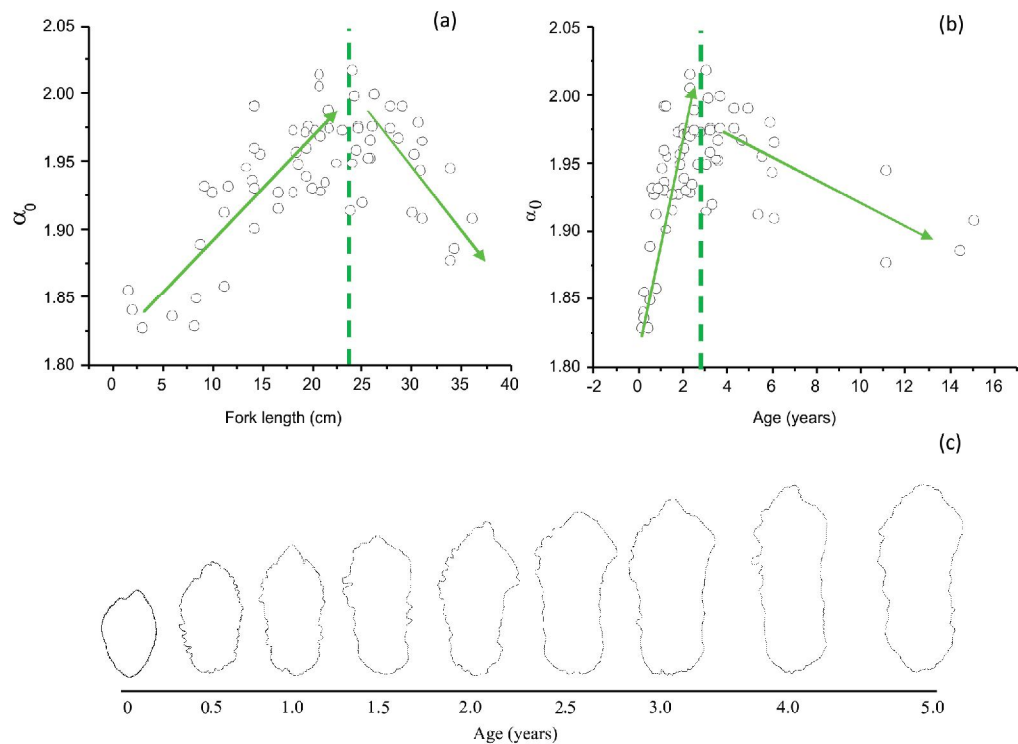
Figure 14: Plot of α_0 parameter against (a) length and (b) age of *M. curema* individuals from the north region of Pernambuco (Brazil). Green arrows represent the variation pattern of the α_0 observed with no distinction between sexes and the green vertical dotted lines indicate the position of the length and age at first maturity estimated by Santana *et al.* (2009). (c) Schematic representation of the roughness variation of the sagittal otolith contour of *M. curema* through age.

the otolith contour during the fish's life caused by alteration of the metabolic rate between reproduction and somatic growth is captured by multifractal analysis. For these species, the changes are reflected in the α_0 parameter, meaning that the sagittal otolith roughness level follows the fish growth, as illustrated in Fig. 14c, while the general shape is kept unchanged.

Note that the determination of first sexual maturity of fish has to date been possible only through costly and cumbersome experimental techniques (SANTANA et al., 2009). Thus the multifractal analysis of otolith contours should prove to be an important tool in fish stock evaluation and management. It is possible that multifractal spectra characteristics may also be related to other fish life history events, and studies could be conducted for otoliths of other vertebrates, such as birds and reptils.
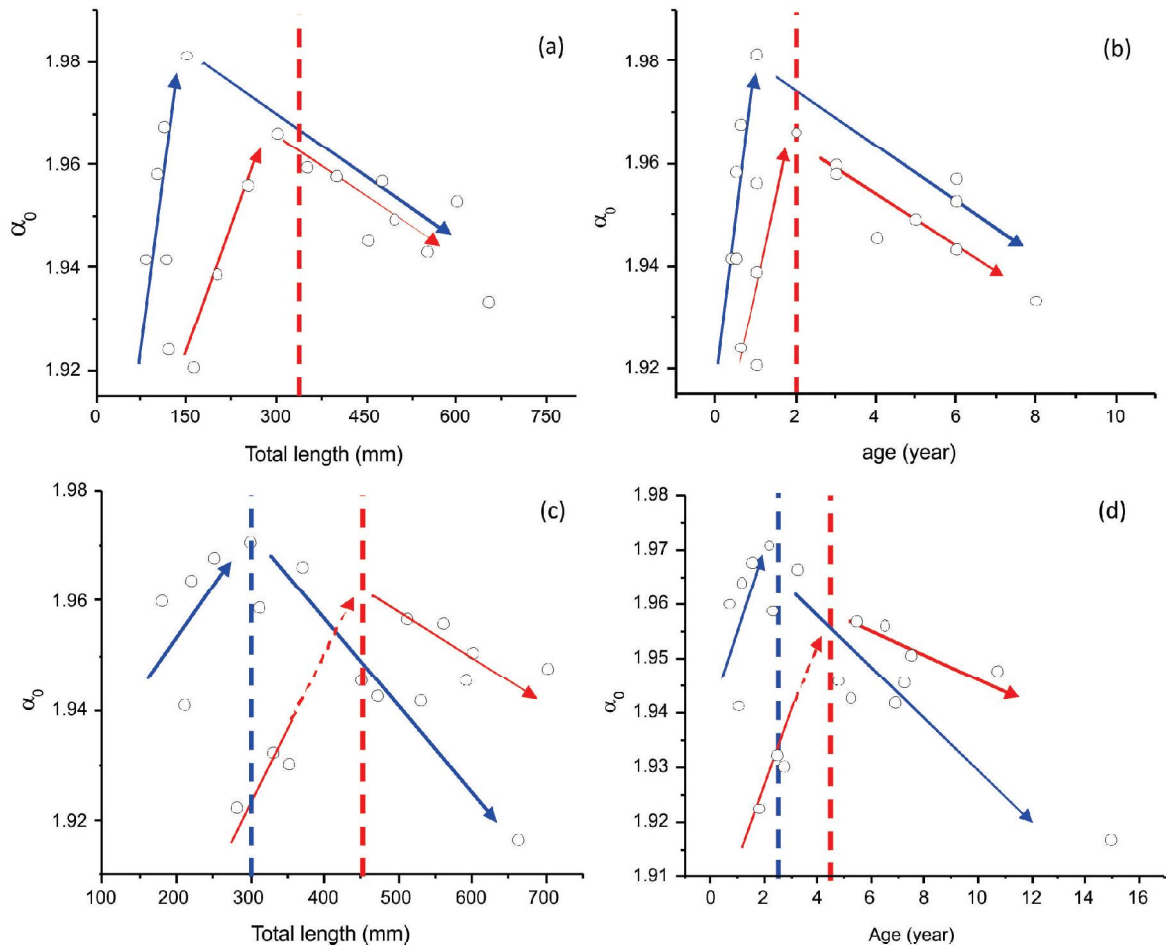
Figure 15: Plot of α_0 parameter against length and age of *M. merluccius* individuals from (a and b) Port de La Selva (Mediterranean population) and (c and d) Galícia (Northeastern Atlantic population). Blue and red arrows represent the variation pattern of the α_0 observed for males and females, respectively. Red and blue lines indicate the position of the length and age of first maturity estimated by different authors for females and males, respectively.

4 Multifractal Parameters in Otolith Shape Classification

4.1 Introduction

It is well known that the shape of sagittal otolith varies widely from simple circular or ellipsoidal forms to rather complex patterns, where a pronounced species dependency is observed (NOLF, 1985). As mentioned in chapter 3, otlith has the function of balancing and hearing. Regarding the latter, the response of a particular sound frequency by the otolith as a transductor depends on its shape (GAULDIE, 2000). This implies that the otolith shape and a certain proportion between the shape and the censorial area are maintained during the fish life (LOMBARTE; POPPER, 1994), since the distribution of otolith morphotypes reflects adaptations to optimize fish survival in the context of different environmental sounds (GAULDIE; CRAMPTON, 2002).

Besides species-specific dependency, the otolith shape often presents clinal variation in respect to geographical location (WORTHMAN, 1979) and/or depth (WILSON, 1985). Lombarte and Castellón (1991) showed that the otolith shape is regulated by the species and in lower degree by environmental factors. Furthemore, Galdie (1988) described other factors that can controll the otolith shape, such as the shape of the optical capsule and the cranium, and the growth discontinuity controlled by the macule. Consequently, the stimuli furnished to the macule are provoked by environmental condition variations, such as photo-period, temperature and feed regime (LECOMTE-FINIGER, 1999). These characteristics make the otolith an excellent structure to be used in marine fish stock studies (GREEN et al., 2009).

Up to date diverse techniques have been employed to quantify this variability, where the use of landmarks (MONTEIRO et al., 2005; PONTON, 2006), elliptical Fourier analysis (STRANSKY, 2005; TRACEY; LYLE, 2006; DUARTE-NETO et al., 2008) and Wavelet analyses (PARISI-BARADAD et al., 2005; LOMBARTE et al., 2006), appear to be the most commonly used techniques. Fractal analysis represents yet another approach to study complex shapes, that has received far less attention in the context of otolith description, with only two studies that use the fractal dimension (calculated by the box-counting method) as a shape descriptor in classification problems (PIERA et al., 2005; DUARTE-NETO et al., 2008). The otolith contour, based on a single fractal dimension, is found to be closer to a line than to an object that fills the two dimensional Euclidian space, as observed by Duarte-Neto et al. (2008) for otoliths of *Coryphaena hippurus* L., that presented values close to unity, varying from 1.19 to 1.25.

In the current context, fractal theory may be used in a more general sense, to quantify the otolith shape complexity at varying scales, however treating the contour as a temporal series instead of a geometrical fractal. Therefore, the first multifractal analysis of the otolith shapes, using otolith images of several species with different shape complexity, is presented here. The contours were mapped onto a time series, using the traveling observer MF-DFA (chaper 2). The multifractal spectra and parameters were investigated to address the question of whether the sagittal otolith contour represents a simple (mono) fractal, or a multifractal structure. Subsequently, the estimated parameters stemming from the multifractal analysis were used as input variables in a traditional multivariate approach, in order to test the usability of the current approach for otolith classification. While this is not the principal objective of multifractal analysis in general (which should rather be understood as a general technique for fluctuation analysis on all scales), this test may be seen as an interface to other traditional quantitative methods employed for otolith analysis, since otolith shape analysis should be based on multishape descritpors (CARDINALE; DOERING-ARJES; GANGNON, 2004; DUARTE-NETO et al., 2008).

4.2   Otolith Sample and Statistical Analysis

Thirty eight otolith images of five species, *Zeus faber*, *Mora moro*, *Merlucius merlucius*, *Ceratoscopelus maderensis*, and *Microchirus variegatus*, with 8 otolith images for the first four species and 6 for the last one, obtained from the image catalog of the project Anàlisi de FORmes d'Otòlits, AFORO (LOMBARTE et al., 2006), were pre-processed to segment the otolith contours. The otoliths of these selected species allow the analysis of a wide range of shape otolith complexity, from a simple circular otolith to a very irregular otolith contour (Fig. 16).
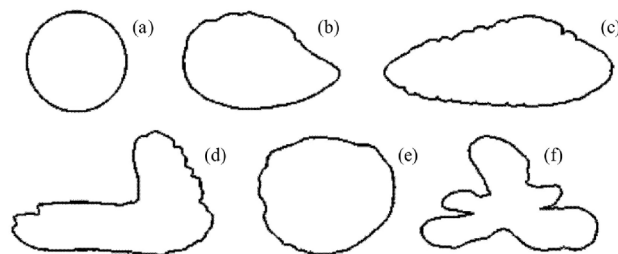
Figure 16: Contour representation of (a) the standard circular shape, and otoliths of (b) *Ceratoscopelus maderensis*, (c) *Merlucius merlucius*, (d) *Mora mora*, (e) *Microchirus variegates* and (f) *Zeus faber*.

The parameter estimates resulting from the multifractal analysis may be used as input variables for a subsequent classical statistical multivariate analysis. Here, we first examine each variable (multifractal parameter estimate) for normality through Kolmogorov-Smirnov Test, and then perform log-transformation if this criterion is not satisfied. Next, the Principal Component Analysis (PCA) is carried out to detect the degree of similarity among the studied otolith complexity, from a multivariate perspective. The principal components that account for most of the variance in the observed multifractal parameters were used for ordering the otoliths in a lower dimension. Linear Discriminant Analysis (LDA) was then applied to verify the potential of the multifractal parameters for species classification. All statistical analyses were performed using the STATISTICA version 7.0 (StatSoft Inc.).

4.3 Multifractal Properties Description

Fluctuations of sagittal otolith contours (Fig. 17) demonstrate multifractal behavior for all species analyzed in the present work, as observed in Figs. 18-20. The generalized exponent $h(q)$ shows a monotonic decay with q (Fig. 18), consistent with the expected behavior for multifractal geometry, and different from a (non-fractal) circle (Fig. 18a), which presented a constant value of $h(q) \approx 1.0$ for all q. This behavior (constant $h(q) \sim 1.0$) was also observed for the shuffled series plots, indicating multifractality of type b) for the otolith contour fluctuations (long-range correlations). A more pronounced decay was observed for *Z. faber* (Fig. 18f), followed by *M. moro* (Fig. 18c), and less accentuated for *M. variegatus* (Fig. 18e; Table 1). The $h(q)$ variability was always higher in the negative part of the q range and almost constant for $q > 0$, except for *Z. faber* and *M. moro*, where the generalized exponent differs widely throughout the q range from one individual to another within species. This behavior is also observed in the $\tau(q)$ *vs* q plot, where $\tau(q)$ values for $q > 0$ are very close for *M. variegatus* and are remarkably overlapped for *M. merlucius* and *C. maderensis* (Fig. 19).

Table 1: Average ($\pm$ standard deviation) multiracial parameters derived from the singularity spectra of the five species analyzed.

Parameters	Species				
	C. maderensis	*M. merlucius*	*M. moro*	*M. variegatus*	*Z. faber*
Δh	0.47 ± 0.13	0.51 ± 0.02	0.75 ± 0.28	0.42 ± 0.12	0.95 ± 0.078
α_0	2.02 ± 0.02	1.95 ± 0.02	1.77 ± 0.14	1.87 ± 0.08	1.86 ± 0.11
$\Delta\alpha$	0.67 ± 0.15	0.76 ± 0.15	1.08 ± 0.34	0.62 ± 0.14	1.29 ± 0.17
$\Delta\alpha+$	0.21 ± 0.04	0.14 ± 0.05	0.45 ± 0.26	0.21 ± 0.06	0.49 ± 0.20
$\Delta\alpha-$	0.46 ± 0.13	0.62 ± 0.11	0.63 ± 0.17	0.41 ± 0.11	0.80 ± 0.04

The singularity spectrum showed a humped shape (Fig. 20), characteristic of multifractal structures in all studied cases. The multifractal parameters obtained from the spectra of all species are presented in Table 1. The average values of α_0 present a narrow range among species, from 1.77 (*M. moro*) to 2.02 (*C. maderensis*), however, with a pronounced difference in α_0 variances for *M. moro* and *Z. faber*, reflecting the fact that some otoliths of these two species present smooth appearance, and others present a rough contour.
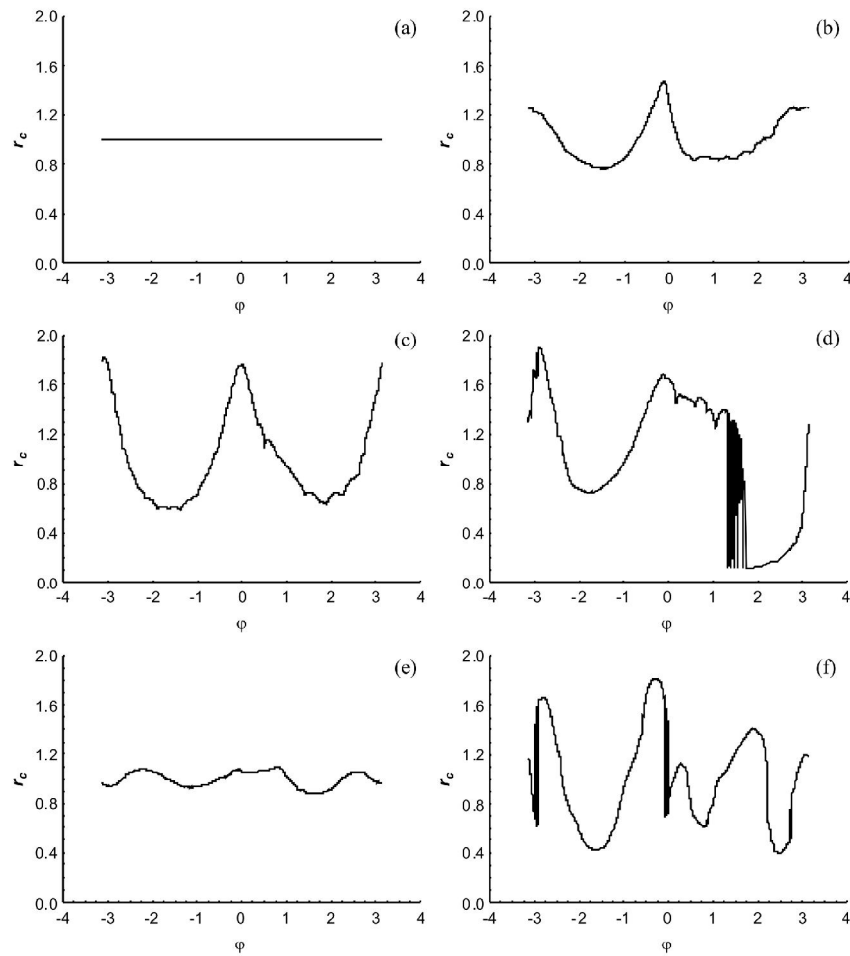
Figure 17: Examples of periodic series of the contour fluctuation derived from the normalized radius (r_c) of the contour at the angle φ for (a) standard circle, (b) *Ceratoscopelus maderensis*, (c) *Merlucius merlucius*, (d) *Mora moro*, (e) *Microchirus variegatus*, and (f) *Zeus faber*.

The *Z. faber* and *M. moro* spectra were wider ($\Delta\alpha = 1.29$, *Z. faber*; $\Delta\alpha = 1.079$, *M. moro*), indicating a "richer"multifractality information content in these contour shapes than in the other more simple otolith structures, reflecting the complexity of the shape, as expected. In turn, *M. variegatus* shows "weaker"multifractal spectrum ($\Delta\alpha = 0.62$), since its shape is closer to a circle. In terms of the average $\Delta\alpha$ values (Table 1), one may order the otolith shapes of the analyzed species by level of complexity: *Z. faber* > *M. moro* > *M. merlucius* > *C. maderensis* > *M. variegatus*. Dominance ($\Delta\alpha-$ and $\Delta\alpha+$) of high (fine structure, $q < 0$) and low (large scale, $q > 0$) Hölder exponent in the shape multifractality spectra were equivalent for the two first species, while the singularity spectra for the other three species were dominated by high exponents (fine structures) (Table 1).
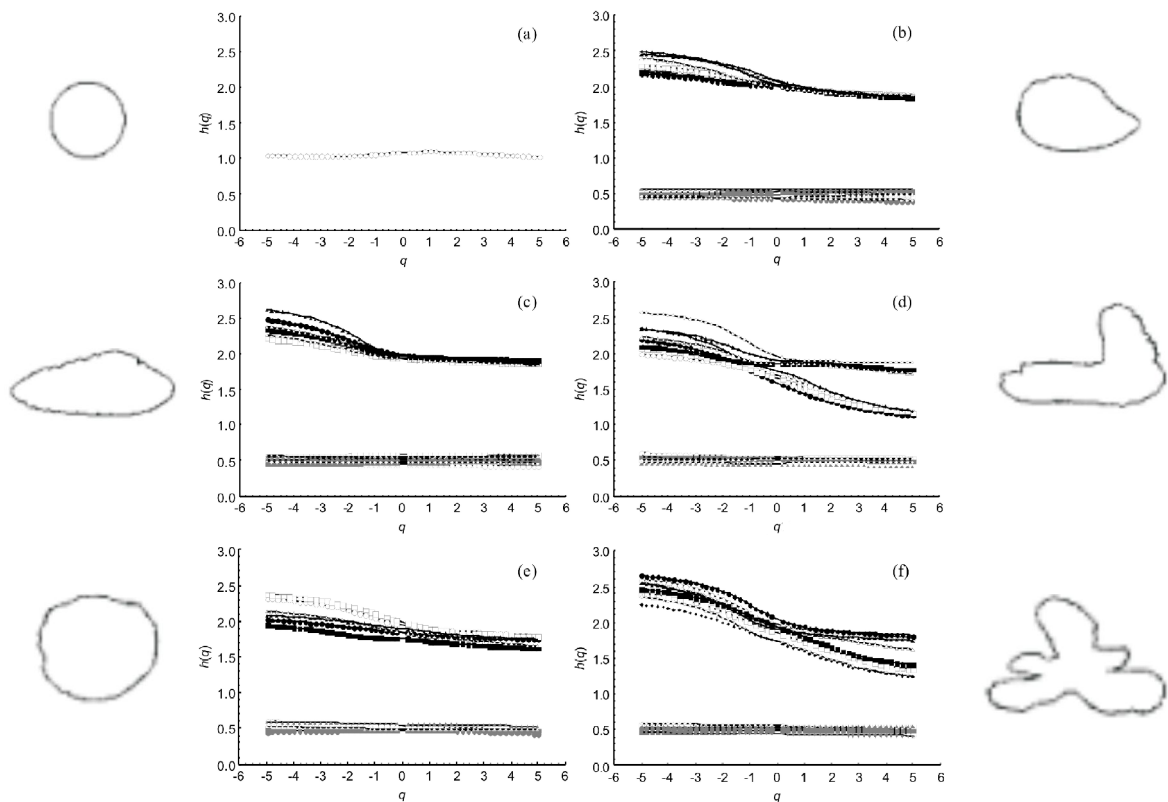
Figure 18: Plot of the qth moment versus the generalized exponent $h(q)$ determined as the slope of the linear regression between $log(\ell)$ and $log[Fq(\ell)]$ for (a) standard circular shape, (b) *Ceratoscopelus maderensis*, (c) *Merlucius merlucius*, (d) *Mora moro*, (e) *Microchirus variegatus*, and (f) *Zeus faber*. Black labels represent the q dependence of $h(q)$ for the original contour series fluctuations, and grey labels correspond to the shuffled series, indicating that $h(q)$ is independent of q.

These results indicate that the otolith contours of *C. maderensis*, *M. merlucius* and *M. variegatus* vary in minor scales, as roughness, maintaining their general shape. *Z. faber* contour shape is very complex, with great variability among individuals, mainly due to differences on large scale, maintaining a similar level of fine fluctuations. *M. moro* and *Z. faber* have similar level of complexity, however, *M. moro* presents greater variability among individuals, both due to large scale and fine structure fluctuations.

4.4   Multivariate Statistical Results

All multifractal parameters presented normal distributions (Kolmogorov-Smirnov Test, $P > 0.05$). Five PCs were obtained from the principal component analysis, however, almost
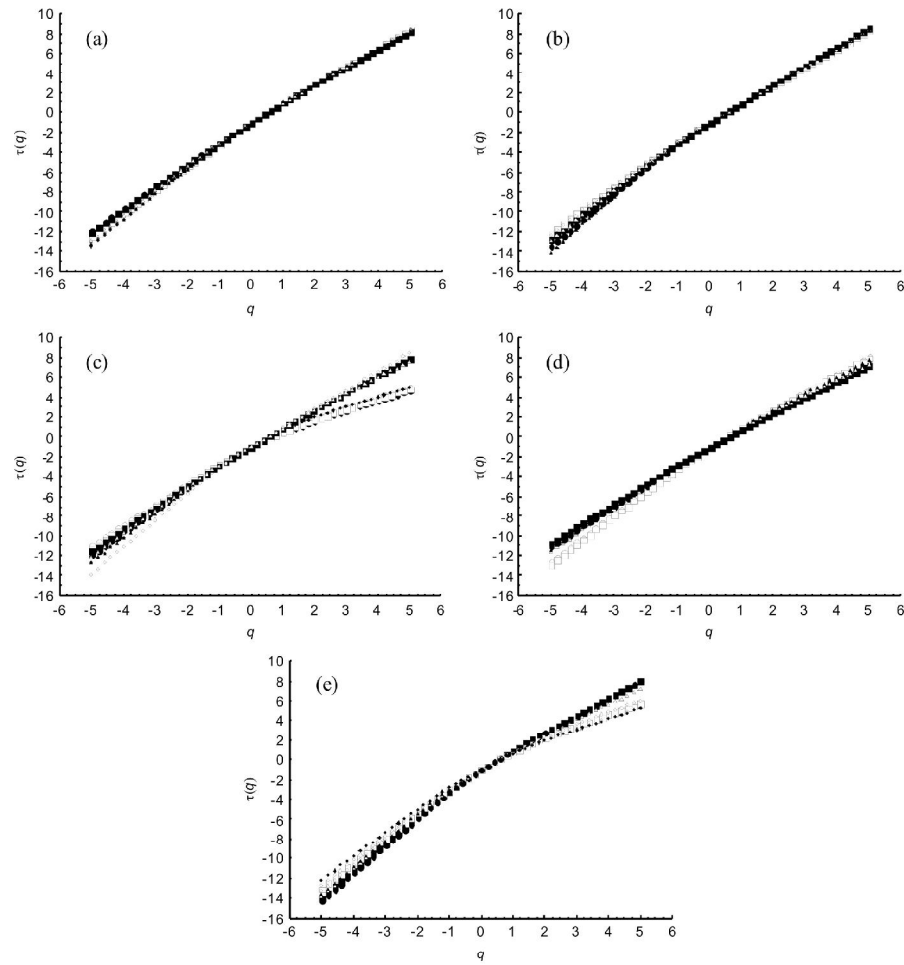
Figure 19: Plot of the qth moment versus the multifractal scaling exponent $\tau(q)$ for (a) *Ceratoscopelus maderensis*, (b) *Merlucius merlucius*, (c) *Mora moro*, (d) *Microchirus variegatus*, and (e) *Zeus faber*.

all of the total variance (91.79%) was found to be explained by the first two PCs. PC1 was strongly correlated (negatively) with $\Delta\alpha$ and Δh, $log(\Delta\alpha+)$. In turn, PC2 was more correlated (negatively) with α_0 and $\Delta\alpha-$ (Table 2).

Consequently, the four quadrants of Figure 21 may be interpreted as follows: 1) simpler shaped otoliths, such as the case of *M. variegatus* and some otoliths of *C. maderensis* and *M. moro*; 2) complex shaped and smooth otoliths, dominated by large fluctuations, such as *M. moro* and some otoliths of *Z. faber*; 3) complex shape, dominated by fine structure fluctuations, where the most of *Z. faber* otoliths are located; and 4) simple shaped otoliths with rough contour and dominated by fine structures, where *M. merlucius* and *C. maderen-*
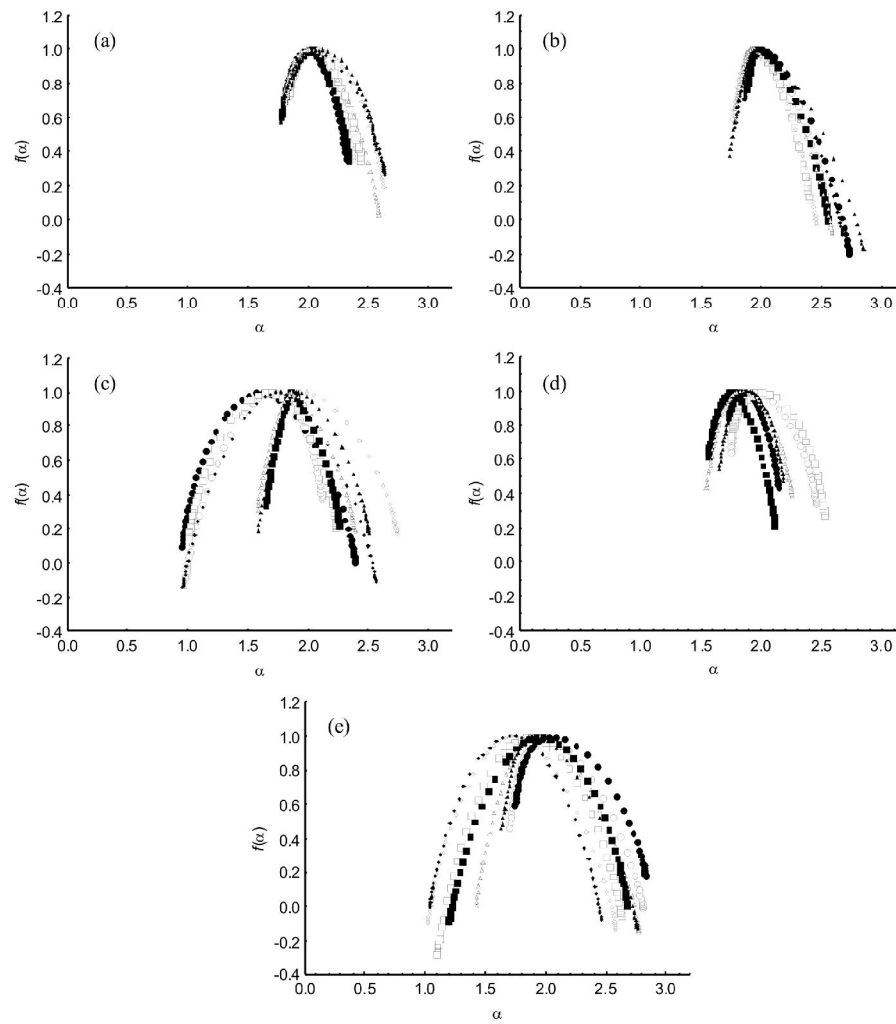
Figure 20: Singularity spectra $f(\alpha)$ for (a) *Ceratoscopelus maderensis*, (b) *Merlucius merlucius*, (c) *Mora moro*, (d) *Microchirus variegatus*, and (e) *Zeus faber*.

Table 2: Principal component and multifractal parameter correlation.

Parameters	Principal Component	
	PC1	PC2
Δh	-0.98	-0.16
α_0	0.64	-0.66
$\Delta\alpha$	-0.99	-0.10
$log(\Delta\alpha+)$	-0.84	0.35
$\Delta\alpha-$	-0.77	-0.59
Eigenvalue	3.64	0.95
Cumulative Proportion	0.73	0.92

sis otoliths were found. Thus, the plot configuration of the studied species otoliths in the

principal component axes corroborates the previous descriptive analysis, drawn from the

multifractal analysis alone.
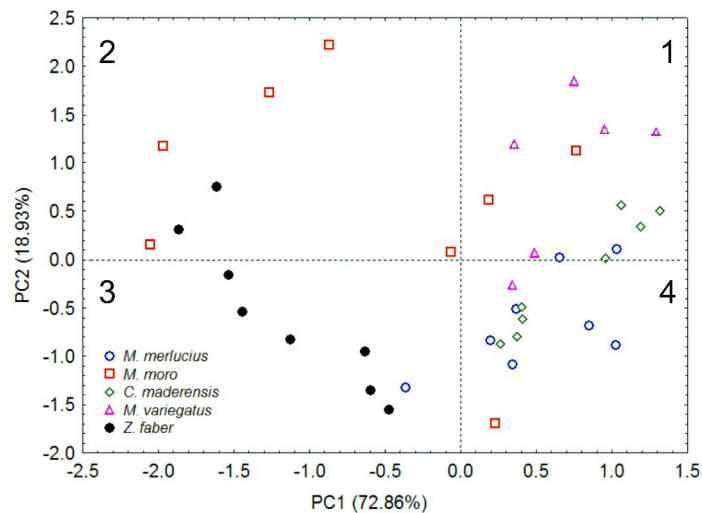
Figure 21: Scatterplot of species otolith scores in the two dimensional principal component plane. The explained variance of each principal component is in parenthesis.

In the same way, Mahalanobis distance calculated between group centroids, submitted to Linear Discriminant Analysis (LDA), showed the same complexity hierarchy of the otolith shape described above, based on $\triangle \alpha$ (Table 3). LDA indicated a relative potential of the multifractal parameters for species separation. The parameter $\triangle h$ was removed from this analysis due its high correlation with $\triangle \alpha$. Overall, 63% of the otoliths was successfully classified (Table 4). Only *M. moro* had a low percentage of correct classification. As described above and shown in Figure 21, this species has a great variability among individuals, both due to large scale and fine structure fluctuations, presenting otoliths very complex as *Z. faber* and simpler as *V. variegatus*.

4.5   Discussion and Conclusions

It was demonstrated in this work that the otolith contours should be characterized as multifractal structures by a hierarchy of exponents, rather than a single fractal dimension. This single exponent represents global properties of a structure and says nothing about the local properties (LOPES; BETROUNI, 2009), although different biological patterns can be adequately characterized by it. Analyzing otolith contours on the basis of multifractal theory

Table 3: Mahalanobis distance (*F statistics;P-value*) between species group centroids.

Species	Z. faber	M. merlucius	M. moro	C. maderensis	M. variegatus
Z. faber	0.00	8.91	4.30	14.58	18.37
	-	*8.1;0.00*	*3.91;0.01*	*13.25;0.00*	*14.31;0.00*
M. merlucius	8.91	0.00	6.07	14.94	15.15
	8.1;0.00	-	*5.52;0.00*	*13.58;0.00*	*11.80;0.00*
M. moro	4.30	6.07	0.00	15.09	10.71
	3.91;0.01	*5.52;0.00*	-	*13.71;0.00*	*8.34;0.00*
C. maderensis	14.58	14.94	15.09	0.00	4.85
	13.25;0.00	*13.58;0.00*	*13.71;0.00*	-	*3.78;0.01*
M. variegatus	18.37	15.15	10.71	4.85	0.00
	14.31;0.00	*11.80;0.00*	*8.34;0.00*	*3.78; 0.01*	-

Table 4: Jackknifed classification matrix of species otoliths obtained trough linear discriminat analysis.

Species	Classification Error	Species				
		(1)	(2)	(3)	(4)	(5)
Z. faber (1)	0.25	6	0	2	0	0
M. merlucius (2)	0.25	1	6	1	0	0
M. moro (3)	0.75	3	0	2	0	3
C. maderensis (4)	0.25	0	0	1	6	1
M. variegatus (5)	0.33	0	0	2	0	4
Total	0.37	10	6	8	6	8

allows the description of the complexity of their shapes in more detail, from fine to large scales, based on the distribution of the multifractal morphological exponents.

The use of the otolith radius normalized by the zero-th harmonic, to extract the fluctuations of the otolith contour, allows reflection about the otolith formation process, based on the multifractal parameters obtained for each species. The otolith biomineralization process starts from the otolith primordium (LECOMTE-FINIGER, 1999), a regular shaped structure, secreted by the inner ear; here represented by the zero-th harmonic circle. The biomineralization continues with the precipitation of calcium carbonate regulated by endogenous rhythm of calcium metabolism (MUGIYA, 1987), resulting in a biomineral creation composed of calcium carbonate crystals contained in a protein matrix (LECOMTE-FINIGER, 1999; ALLEMAND et al., 2007). If the calcium precipitation is homogeneous along the contour, i.e. with the uniform probability of aggregation along the otolith boundary during the biomineraliza-

tion process, then it may be expected that the shape of an older individual should be very similar to the initial shape (a circle).

It follows from the above reasoning and the estimated multifractal parameters, that *C. maderensis* and *M. variegatus* contour shape did not substantially change from the initial shape during the biomineralization process, reflecting both a uniform (or isotropic) probability of calcium carbonate aggregation along their otolith contour, and a homogeneous aggregation rhythm among specimens. It was found that $\Delta\alpha$ for *M. merlucius* is greater than for the two former species, followed by *M. moro* and *Z. faber*, suggesting that the increase of width of the range of the singularity spectrum reflects increase of anisotropy of the aggregation probability along the contour. More precisely, this range reflects the noise corresponding to the fluctuations of the contour, caused by the protrusions and cavities in the otolith shape, which represent sites in the otolith with low and high aggregation probability.

Another possible conclusion is that as elevated $\Delta\alpha-$ values reflect enhanced small-scale fluctuations (roughness, perhaps stemming from temporal fluctuations of the local deposition probability), as observed for *M. merlucius*. Possibly, multifractal parameters may be used as input ingredients for future microscopic growth otolith models, reflecting the degree of heterogeneity of aggregation probability.

Fractal dimension of otolith contour was estimated by Piera et al. (2005) and Duarte-Neto et al. (2008) using box-counting method. However, as highlighted in chapter 2, this technique has been demonstrated to be rather problematic for the multifractal approach. On the other hand, the methods commonly used for multifractal analysis of time series do not present problems (KANTELHARDT et al., 2002; MUZY; BACRY; ARNEODO, 1991; OSWIECIMKA; KWAPIEN; DROZDZ, 2006). Among them, MF-DFA yields reliable results both for large negative q and for shorter signals (OSWIECIMKA; KWAPIEN; DROZDZ, 2006), besides having lesser requirements for computational power (KANTELHARDT et al., 2002). This method has demonstrated to be rather satisfactory for analysis of otolith contour fluctuations in the current work, and no problems have been experienced in the implementation. As commented in chapter 2, the combination of this multifractal methodology with the Fourier regular analysis

brings two distinct advantages to the contour multifractal analysis: invariance to size, and multiple values for a single angle. However, differences in image resolution could be a limitation for its use, since a higher resolution should exhibit more particularities of the images. To avoid possible complications due to such an effect, all the images analyzed here were taken at the same resolution.

It was demonstrated here that the multifractal properties may be used for species discrimination, although this is not the main focus of multifractal analysis, nor does it represent the sole objective of the current work. Future research efforts shall be directed to study the effect of additional features, such as temperature, feeding, and other environmental variables, in the attempt to relate the differences observed in the multifractal parameters, with those features. A user friendly program that implements multifractal analysis as proposed in this work is available at the site http://www.pgbiom.ufrpe.br/downloads/calcradius/, since the composite procedure described here is in fact rather general (it is not limited to otolith shape analysis), and may be carried out for multifractal analysis of any closed contour.

5   Multifractal Analysis of Microscopic Aggregation Growth Model

5.1   Introduction

Simulation growth models are widely used to describe many different growing natural structures, constructed to reflect the essential features of specific growth phenomena, that are, however, shared by other phenomena in nature (VICSEK, 1989). Scaling laws, mono and multifractal properties and phase transitions that are intrinsic to the growth of artificial structures represent examples of features that can be compared with experimental data observed during the growth of natural structures, helping to understand their growth process on the base of simulations. For instance, the physics of far-from-equilibrium growth phenomena represents one of the main fields where fractal growth models are applied. The choice of the most appropriate model to explain the growth of any given phenomenon is an important step in order to identify the minimal set of factors that govern the growth process and the formation of large clusters by aggregation of identical subunits (particles) in nature, allowing one to investigate the relevance of each factor.

A wide variety of materials, like colloids, polymers, aerosols ceramics, glasses and thin films are formed by aggregation (BARABÁSI; STANLEY, 1995). Aggregation is the process when identical particles are joined into clusters according to some rule. To represent this process, simulations are usually carried out on regular lattices and the diameter of the particles is assumed to be the same as the lattice spacing, but many variations of this basic idea

can be simulated. Two main geometries are most commonly considered: a) aggregation is conducted along a surface, or b) it starts from a single seed particle. Aggregation almost always leads to ramified structures with fractal geometry. An important characteristic of the simulations is that the relevant details of the models are governed by the physics of the aggregation process being simulated. In particular, the trajectory of the particles plays a decisive role (VICSEK, 1989; MEAKIN; FAMILY; VICSEK, 1987; BARABÁSI; STANLEY, 1995).

One characteristic that is common to all growth process is the existence of "active" and "frozen" regions over the cluster surface. The first region comprehends, usually, the outer part of the surface that is able to receive new particles and the "frozen"region represents the union of all parts hidden by (or behind) the "active" part (PLISCHKE; RÁCZ, 1984).

Examples of the classical growth models are the Eden model (EM), ballistic deposition (BD) and diffusion limited aggregation (DLA). Eden model was introduced in 1961 by M. Eden to describe the formation of cell colonies, e.g. bacteria and tissue cultures (EDEN, 1961), and is defined as follows. On a lattice, a particle or a surface seed is placed at the origin. A new particle is added at any site chosen randomly around the perimeter of the seed, forming a two particle cluster. After many such aggregation steps, performed at randomly chosen sites at the perimeter of the existing cluster, the model generates a compact cluster with a rough perimeter (Fig. 22A). The BD model was introduced in turn to model colloidal aggregates (BARABÁSI; STANLEY, 1995). In this model, the particle moves on a straight trajectory until it encounters the growing cluster, and sticks to its perimeter irreversibly (VICSEK, 1989). Here, the seed can be a surface (Fig. 22B) or a single particle (Fig. 22C).

The standard DLA model was first introduced by Witten and Sander in 1981 and it is based on the following process: a seed particle is fixed at a central point of the substrate and another particle is released from a random position away from the seed. The released particle moves according to a Brownian trajectory until it reaches one of sites on the perimeter of the seed, when it is fixed, forming a cluster of two particles. This process is carried out repeatedly (Fig. 23). The probability of growth of a certain site of the perimeter

corresponds to the probability of a random walker to visit this site. This probability (u) obeys the steady-state diffusion equation

$$\nabla^2 u = 0 \tag{5.1}$$

where $u = 1$ at infinity, $u = 0$ in peripheral sites. The probability for a peripheral site to be visited is proportional to the flow on this site, ie. $\rho \propto \nabla u$. On the square lattice, DLA model can be described by the discrete Laplace equation

$$u_{i,j} = (u_{i-1,j} + u_{i+1,j} + u_{i,j+1} + u_{i,j-1})/4 \tag{5.2}$$

The resultant cluster of a DLA process is characterized by a branched shape (Fig 22D).
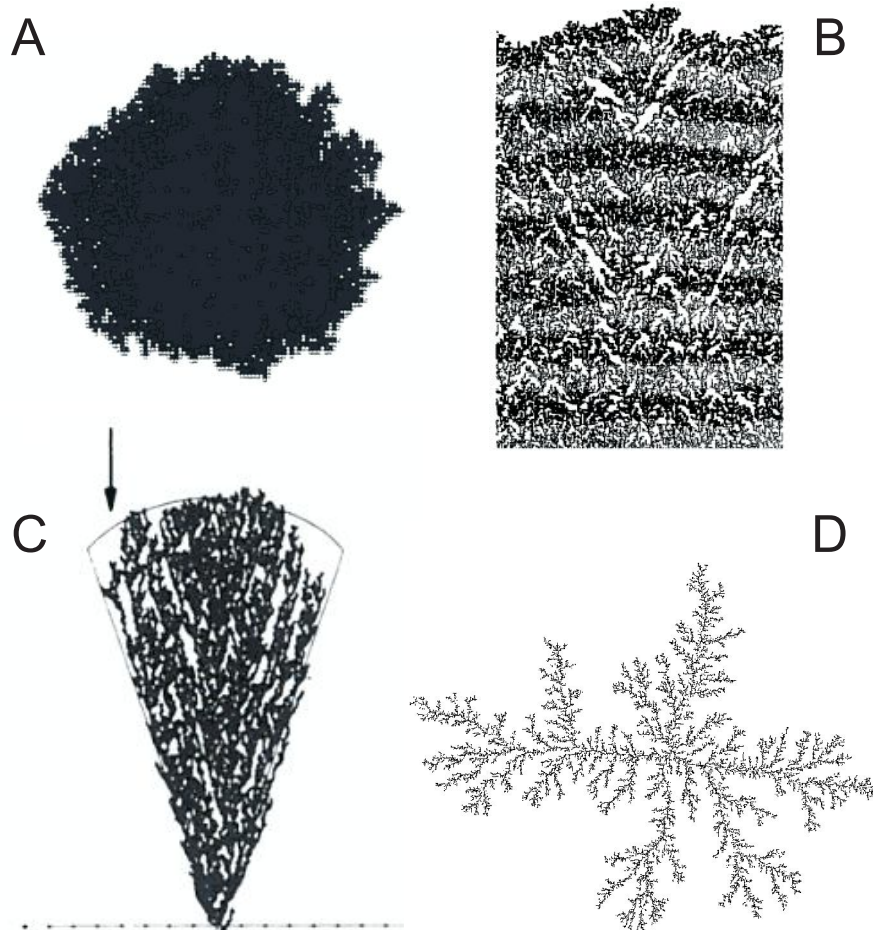
Figure 22: (A) A Eden cluster consisting of 5000 particles started from a single seed (VIC-SEK, 1989); (B) Ballistic deposition cluster with 35,000 particles started from a surface (BA-RABÁSI; STANLEY, 1995); (C) off-lattice balistic aggregates with 180,000 particles started from a single seed particle (VICSEK, 1989); and (D) square-lattice diffusion limited aggregates with 50,000 particles.

In turn, the generalization of the DLA model proposed by Batchelor and Henry (1992), takes into account the local sticking probability s defined as

$$s = \alpha_p^{3-B} \tag{5.3}$$

where the parameter $0 < \alpha_p < 1$ corresponds to the local "surface tension", and $B \in 1, 2, 3$ is the number of neighboring sites seen by the incoming particle.
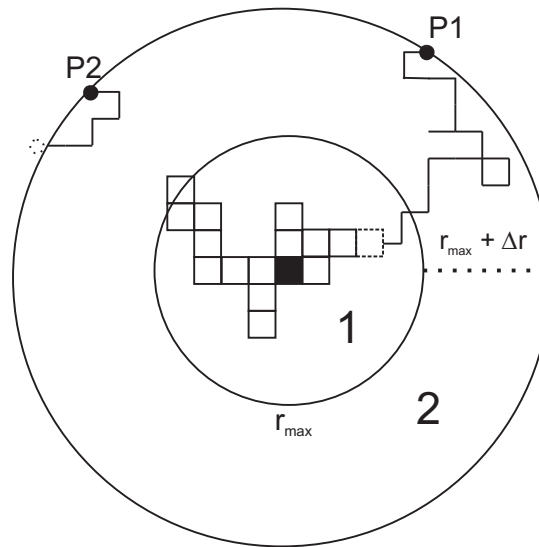
Figure 23: Schematic representation of a square-lattice diffusion limited aggregation process. In step 1: a seed particle (black pixel) is fixed at a central point of a circle with radius equal to r_{max}. Particles are released one by one from a random position on the circle, and move according to a Brownian trajectory to reach one of the 4 nearest neighbors of the seed, when it is fixed, forming a cluster (white pixels). In step 2: a Δr was added to the initial radius, aiming to keep a uniform distance between the initial position of the new particle and the cluster during the aggregation process. A new particle is released when the previous particle attach to the cluster (as show for P1) or reaches the outer circle (being removed) (as show for P2).

DLA patterns are fairly common in nature, including biological phenomena, such as bacterial, neural and stony coral growth (BARABÁSI; STANLEY, 1995; KAANDORP et al., 1996; MERKS et al., 2003). Due to the simplicity of the algorithm, DLA model should permit simulations and evaluation of diverse environmental, morphological and physiological scenarios simply by changing the original conditions that characterize the standard DLA model definition described above. Indeed, this model is easily generalized, and hence it plays a paradigmatic role in the field of kinetic growth phenomena (HANAN; HEFFERNAN, 2012). Because of this generality, we use the DLA model in our simulations to generate aggregation-

based structures from different growth conditions, and then, the multifractal properties of their perimeter fluctuations were evaluated using the "traveling observer" MF-DFA approach (described in chapter 2).

5.2 Simulations

The simulations were performed using a program written in C language divided in tree main steps: 1) the growth of the aggregates, 2) the aggregate contour tracing, and 3) multifractal analysis of the contour.

5.2.1 Step 1: the growth of the aggregates

The probability of growth , directional bias in movement, and the probability of launching particles were modified with respect to the standard DLA model. Based on these modifications, four scenarios were evaluated:

1. α_p varied from 0.01 to 1.0 with step of 0.01.

2. In this scenario, for each α_p value, ρ_1 (probability of motion in a given direction i, equivalent to the particle flow) varied from 0.1 to 0.9 with step of 0.1. The probability of motion for each of the other three directions was taken to be $\rho_i = (1 - \rho_1)/3$.

3. Here, two perpendicular directions probabilities were considered. For each α_p value, probability of motion in two directions were changed, ρ_1 and ρ_2, varying from 0.1 to 0.9 with steps of 0.1.

4. In this scenario, instead of launching particles uniformly from a distant circle, von Mises distribution was used to simulate preferential source of particles (see Appendix A). For each α_p value, the location (μ) and concentration (κ) parameters of the von Mises distribution were modified. Two values of μ were considered $3\pi/2$ and $5\pi/4$, and κ varied from 8 to 0.5, with step of 0.5, for each location.

For each of the scenarios first a seed was placed at the center of a 512 x 512 matrix. The new particles were then released from a random position (according to a uniform, or a von Mises distribution) on a circle with initial radius of 100, after which they move randomly in four directions (up, down, left and right), each one with a given (pre specified) probability. Particles that reach the launching circle are discarded, and the ones that reach the growing cluster perimeter stick with probability s (Eq. 5.3), or continue moving with probability $1 - s$. Every time that a particle sticks to the cluster, the size of the cluster radius (maximum displacement from the center) is compared with the launching circle radius, which is in turn increased as to maintain a minimum distance of $\Delta r = 10$ (Fig. 23). As opposed to the standard DLA model, this choice of a small cluster to launching circle distance was made to maintain chambers of size comparable to that of the cluster itself, that is commonly encountered in nature. Finally, the aggregation process terminates when the cluster reaches the size of 50,000 particles. Each growth condition was repeated 20 times to minimize variations due to random noise.

5.2.2 Step 2: the aggregate contour tracing

Once the cluster was obtained, the matrix containing information on cluster particle positions was used to extract the contour of the aggregate. To trace the contour we used 8-connected boundary pattern as shown in Fig.24. In practice, the pixels that formed the contour were the black pixels connected with other black pixel and with at least one white neighbor.

5.2.3 Step 3: multifractal analysis of the contour

This step was carried out using the procedure described in chapter 2. The x and y coordinates of the cluster contour pixels were used to determine the radius of each contour point and the average radius of the structure (zero-th harmonic), used to normalize the individual contour pixel radii. Thus, for each set of input parameters a series of normalized radii from $-\pi$ to π was obtained. We fixed the degree of the polynomium that is fitted to the
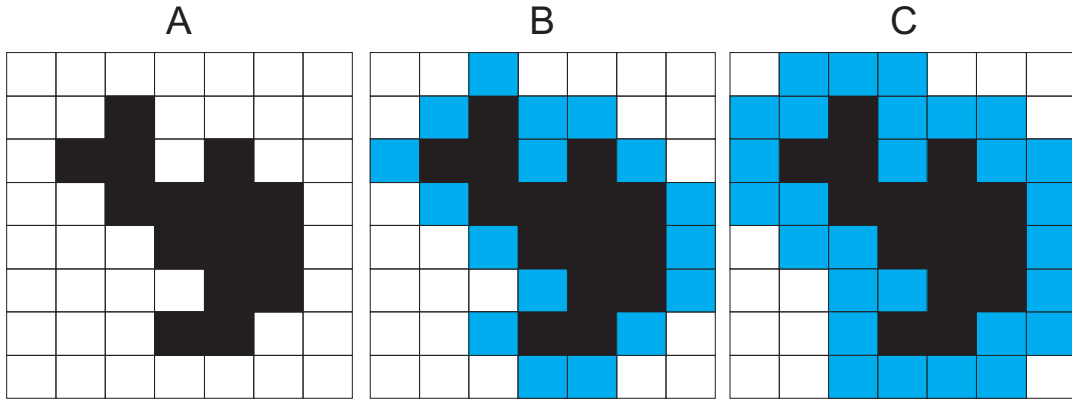
Figure 24: Representation of the contour tracing procedures of an (A) object (black pixels) by a (B) 4-connected and (C) 8-connected boundary pattern. The contours are shown in blue.

segment ν in Equation 2.3 to one, and the q values in Equation 2.4 varied between -10 to 10 with $\Delta q = 1$.

As described in chapter 2, the generalized exponent $h(q)$ is the slope of the linear regression between $log(\ell)$ and $log(F_q(\ell))$. The value of $h(q)$ is very sensitive to the choice of the range of points that are used for fitting, manly to those that represent very small and very large scales. If all points in the log-log plot lay on a straight line, then the choice of range would not alter the slope. However, if there are outliers that deviate from the line, then removing these points would lead to a substantial change in the $h(q)$ value. For all data series, a stable estimation of $h(q)$ is desired, so in order to avoid problems with outliers one could make a visual choice of the range or consider a minimum value of goodness of fit, using, for example, the coefficient of determination R^2.

Here, a more robust protocol is used, quantifying the effect of each point in the log-log plot by determining the leverage effect through DFBETAS regression diagnosis (DAMOURAS et al., 2010)

$$DFBETAS(i) = \frac{h(q) - h(q)_i}{std(h(q)_i)},$$
(5.4)

where $h(q)$ is the slope of the log-log plot with a wider range and $h(q)_i$ is the slope of log-log plot at the reduced range obtained by truncating the data at point i. DFBETAS are distributed as $t(m-2)/\sqrt{m}$, where $t(m-2)$ is the t-distribution with $m-2$ degrees of freedom and m is the number of segments (scales). Based on this distribution it is possible

to calculate a p-value for the statistics and then determine if the point being evaluated has significant effects ($p < 0.05$). So, we proceeded as follows:

1. First the linear regression was conducted using the entire range. If R^2 value was found to be lower than 0.94, we performed the next step, and if it was found to be greater than or equal to 0.94, we considered that the fit was adequate;

2. The DFBETAS diagnosis was conducted successively for the points on the extremes, alternating between smaller and larger scales. This procedure is terminated when R^2 of the new fit reaches 0.94, or if the number of segments is reduced to 25.

This procedure leads to a stable estimate of the slope in the sense that it is not overly reliant on small or large segment sizes. The rest of the procedure followed the routine describe in the chapter 2. The behavior of the cluster growth in each scenario was evaluated considering both the qualitative changes in the cluster shape and the multifractality of their perimeter fluctuations.

5.3   Results and Discussion

5.3.1   Microscopic aggregation growth as a function of the "surface tension" - Scenario 1

5.3.1.1   Morphological changes

All clusters obtained here (Fig. 25) are isotropic or converge to an isotropic shape with the increase of the number of particles, since the particles are released from an uniform random position and move according to a Brownian trajectory. Clusters obtained with a low α_p value are more compact, resembling an Eden-like cluster, and the closer α_p gets to unity, the more standard DLA-like the cluster becomes.

For DLA growth, parameter α_p is analogous to the "surface tension" (MEAKIN; FAMILY; VICSEK, 1987; BATCHELOR; HENRY, 1992).This analogy is often related to fluid-fluid interaction, when the shape of the surface of a fluid depends of the properties of the fluid or surface

that is in contact, such as the viscous fingering, studied by Meakin et al. (1987). The reference to the effect of "surface tension" on the form of aggregates was made early by D'Arcy Thompson in 1917 to describe the form of aggregates of cells and tissues (THOMPSON, 1992). However, independent of the kind of phenomenon, the effect of surface tension results in minimizing the area that the present conditions and circumstances of growth will permit, i.e. the possible reduction of the surface in contact, reflecting minimization of potential energy of the system (equilibrium state). It can be seen on Figure 25 that the lower α_p values yield stronger (or more complex) particle connections, since the particle needs more neighbors to be fixed to the cluster, resulting in a more smooth, reduced surface. Increasing this parameter the clusters start to present a more rough border with protrusions and cavities, increasing the surface in contact with the environment. Hence, the way that particles connect one to another appears to be an important characteristics that controls the shape of a structure in terms of the roughness of the border and surface.

This characteristics is observed during the biomineralization process in nature, especially during the construction of crystalline polymorph structures composed of calcium carbonate: calcite, aragonite and vaterite (Fig. 4). Mukkamala et al. (2006) demonstrated how the environment controls the mineral phase and the growth of the mineral in terms of its shape (including the border appearance) and size in the final structure. Modifications of the environmental conditions change the morphology of calcium carbonate crystal and, consequently, the way that crystals and their molecules aggregate. Besides the environment, the protein matrix (that is regulated genetically) is functionally essential in the process of biomineralization, controlling the successive stages of biomineral creation and their resulting shapes (ALLEMAND et al., 2007). For example, experiments suggest that with reduction of the gene starmaker activity the otolith of zebrafish presented a rough surface, rather than the normal smooth appearance (SÖLLNER et al., 2003). It seems that modification of this gene affects the level of protein formation, and hence, causes changes in the structure of the protein matrix and calcium carbonate crystal aggregation.
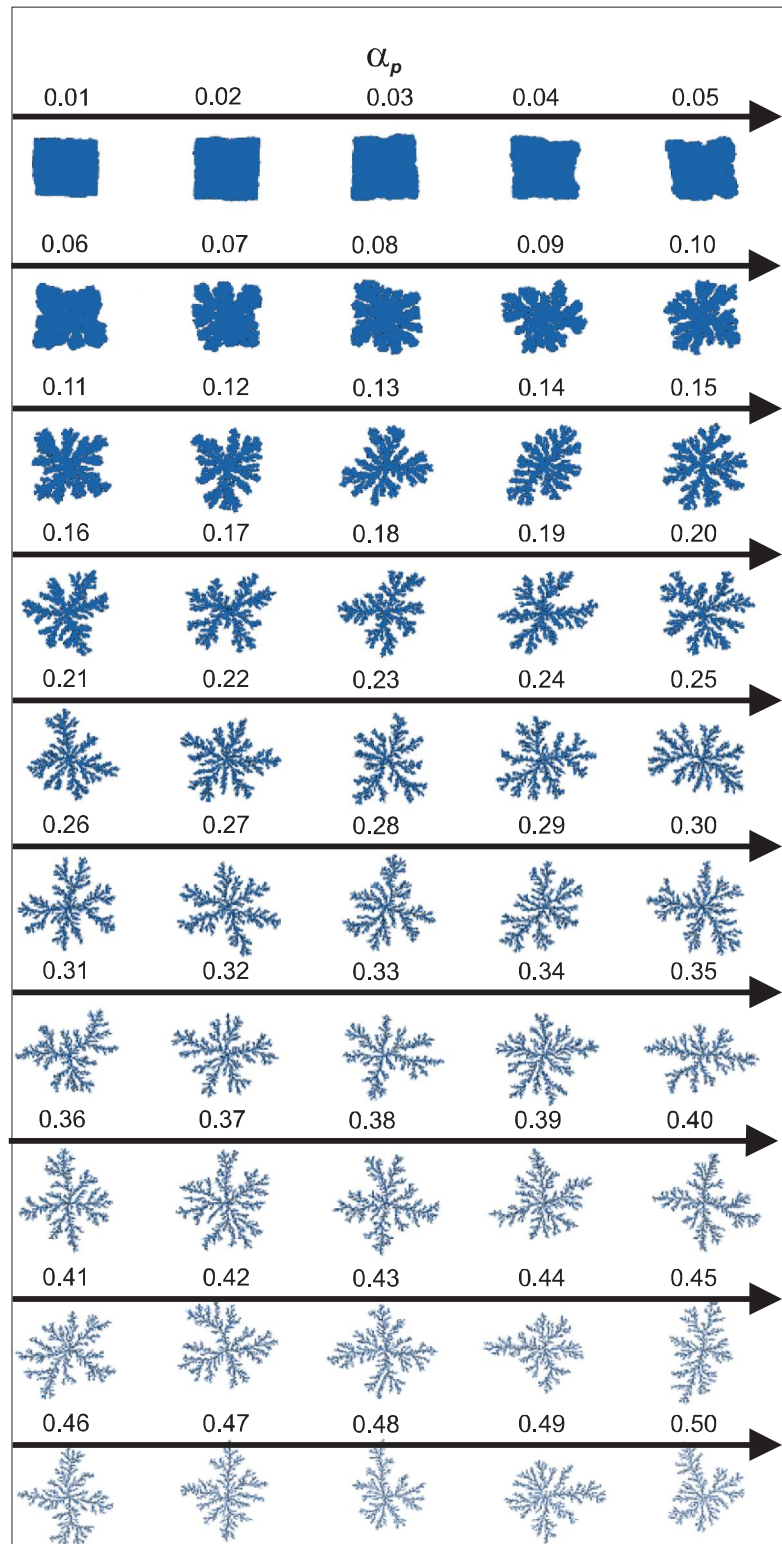
Figure 25: Morphological diagram of clusters with 50,000 particles aggregated with different "surface tension" (α_p values).

5.3.1.2 Multifractal properties

The contour fluctuation of the aggregates showed multifractal behavior (Fig. 26) for the entire range of α_p. The generalized exponent $h(q)$ shows a monotonic decay with q (Fig.

26A), $\tau(q)$ shows two different regimes for negative and positive q (Fig. 26C) and the singularity spectrum showed a humped shape (Fig. 26D). Both kinds of multifractality are present in the cluster fluctuations, multifractality due to a broad probability density function and due to different long-range correlations for small and large fluctuations, since the shuffled series demonstrated weaker multifractality than the original ones (Fig. 26B).
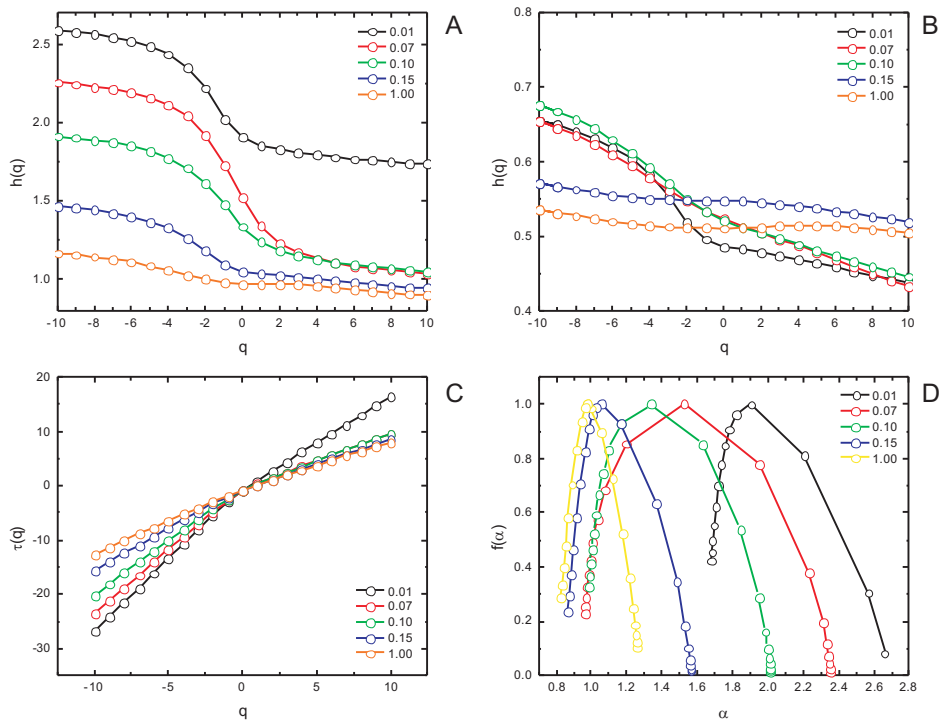
Figure 26: Plots of the qth moment versus the generalized exponent $h(q)$ determined as the slope of the linear regression between $log(\ell)$ and $log[Fq(\ell)]$, obtained from (A) the original series and (B) the randomized series, (C) the qth moment versus the multifractal scaling exponent $\tau(q)$, and (D) the singularity spectra $f(\alpha)$ for different values of α_p.

Figure 26 shows that the multifractality of the aggregates depends of α_p, becoming weaker as the standard DLA limit ($\alpha_p = 1$) is approached. Weak multifractality of DLA was observed in several studies both with respect to growth probability measure (NAGATANI, 1988) and local density of multifractal geometry (VICSE; FAMILY; MEAKIN, 1990; HANAN; HEFFERNAN, 2001, 2012). The strongest multifractality was observed for $\alpha_p = 0.07$ (Fig. 26D and Fig. 27B), and the peaks observed for $\Delta\alpha$, $\Delta\alpha-$ and $\Delta\alpha+$ in Figures 27 B,C and D correspond to this value.

In fact, if one considers the sticking probability α_p as the parameter which brings about

perturbations in the contour (equivalent of temperature in thermodynamics), the central position α_0 of the singularity spectrum as the order parameter (the higher the value of this parameter, the smoother the contour), and $\Delta\alpha$ as the response function (derivative of the order parameter), than curves displayed in Fig. 27 A and B are strikingly reminiscent of their thermodynamic equivalents (e.g. magnetization and susceptibility, or density and compressibility). From this point of view the current results suggest that $\alpha_p = 0.07$ is a(n) (effective) critical point representing a phase transition between an "ordered" phase (rather smooth contour on large scales, but with pronounced multifractality), and a "disordered" phase (a rough contour on large scales, but of low multifractality). The otoliths showed in the previous chapter can be therefore considered to present contours falling within the ordered phase, while standard DLA clusters and, possibly stony corals, fall into the disordered phase region.

It follows that multifractal parameters from the current approach may be used to express quantitatively the level of organization of particles in natural aggregates, and bring about remarkable similarities with behavior of other model systems of statistical physics. In particular, the existence of a possible "phase transition" suggests a new venue of research regarding contour shapes, and perhaps promising a whole new level of their understanding.

5.3.1.3 Finite Size Scaling

In figure 26, we showed a slight dependency of $h(q)$ on q, representing a weak multifractality of the DLA-like cluster contour fluctuations ($\alpha_p = 1$) with 50,000 particles, as observed in several works with different measures and cluster size (NAGATANI, 1988; VICSE; FAMILY; MEAKIN, 1990; HANAN; HEFFERNAN, 2001, 2012). Concerning the multifractality of the DLA-like structure, there are two different opinions among the authors: 1) the growth of DLA-like objects deviates from a simple power law and requires a hierarchy of exponents; and 2) the DLA-like objects present strong finite-size effects and this is believed to be the cause that simple scaling cannot accurately describe these structures, but should hold asymptotically (LAM, 1995).
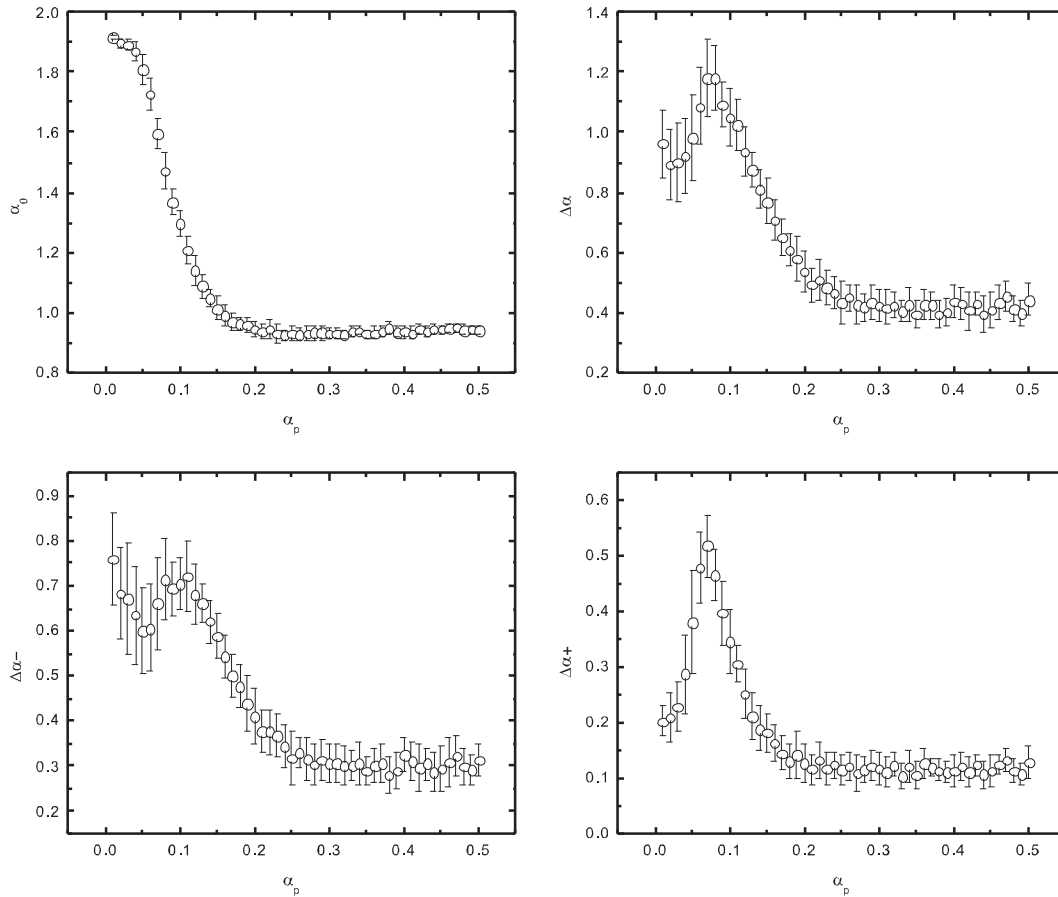
Figure 27: Variation of the multifractal parameters as a function of the "surface tension" parameter α_p. Open circles correspond to the mean values and bars to $\pm$ the standard deviation.

In this context, the existence of finite-size effects on the multifractal parameters of the contour fluctuation of the aggregates is analyzed here. For this, growth of clusters of different sizes L (2000, 10000 and 50000 particles) were simulated, using the same procedure as described above. On the resulting clusters, we applied the "travelling observer"MF-DFA approach and the multifractal parameters α_0, $\Delta\alpha$, $\Delta\alpha+$and $\Delta\alpha-$ were obtained from the singularity spectra.

The "order parameter"and "response function"behavior observed for contour shapes in the previous section is reminiscent of a (smooth) second order phase transition. While the order parameter in the thermodynamic limit is nonzero below the critical point, and zero above the critical point, finite size effects induce a "tail"in the order parameter curve, as shown in Fig. 28, and a maximum (or a cusp) in place of divergence of the response function. The type of transition (universality class) is characterized by critical exponents,

which govern the behavior at the critical point (STANLEY, 1971; BRANKOV, 1996).

While considering finite size systems "destroys"typical phase transition behavior of order parameter and response functions, the concept of finite size scaling helps extracting the phase transition characteristics from finite system behavior (BRANKOV, 1996). The most used scaling functions are as follows:

1. $M \propto |t|^{\beta}$ (thermodynamic limit in the vicinity of the critical point) or $M = L^{-\beta/\nu} g_M(tL^{1/\nu})$ (finite-size system);

2. $\chi \propto |t|^{-\gamma}$ (infinite system) or $\chi = L^{\lambda/\nu} g_\chi(tL^{1/\nu})$ (finite-size system);

3. $C \propto |t|^{-\alpha}$ (infinite system) or $C = L^{\alpha/\nu} g_C(tL^{1/\nu})$ (finite-size system);

4. $\xi \propto |t|^{-\nu}$ (infinite system) or $\xi = L g_\xi(tL^{1/\nu})$ (finite-size system);

where M, χ, C and ξ are, respectively, the magnetization (order parameter), magnetic susceptibility, heat capacity and correlation length, and β, γ, α and ν are the corresponding critical exponents that govern the behavior of the system near the critical point. The variable t is defined as $(T - T_c)/T_c$, where T is temperature and T_c is the temperature at the critical point.
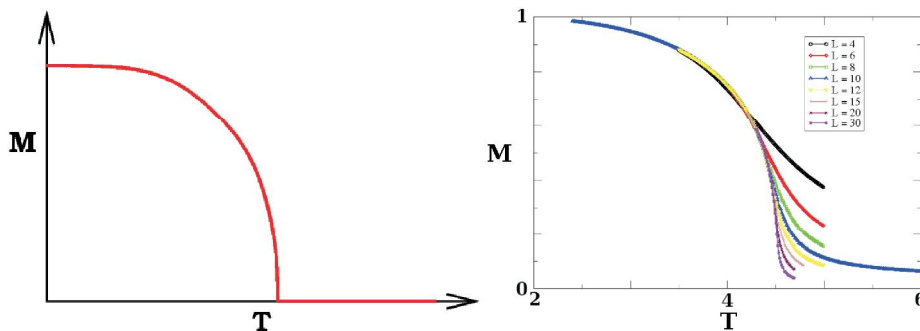
Figure 28: Left: Magnetization in the thermodynamic limit. Right: Magnetization in a finite size system with different system sizes (from Pro-seminar in Theoretical Physics by H. G. Katzgraber).

A strong dependency of the $h(q)$ behavior (Fig. 29A) and the multifractal spectrum (Fig. 29B) on the cluster size is observed for the contour fluctuations, indicating pronoun-

ced finite-size effects. Clusters with different sizes present different multifractal patterns. However, independent of the cluster size, multifractality was always obtained.

Lam (1995) advocates the view that the multifractality of DLA measures, such as growth probability and local and radial densities, are highly influenced by finite-size effects on the basis of a variety of numerical results. Examining the present results for the DLA-like clusters, there seems to be no clear difference between the multifractality of clusters with 10,000 particles (closed blue squares in Figure 29) and 50,000 particles (closed blue circles in Figure 29), which indicates a collapse of the multifractal properties of "active" contour fluctuation of the DLA for larger clusters. This suggests that the normalization used in the current "traveling observer"MF-DFA approach, with respect to the zero-th harmonic reduces (or eliminates) finite size effects for DLA clusters above roughly 10000 particles.

Figure 30A shows some sample images of the growing structures for different cluster sizes, and different α_p values. These images represent the clusters from some (arbitrarily chosen) reference points of the plot of α_0 versus α_p (Fig. 30B), for different sizes: maximum value of α_0, 90% of the maximum, average α_0 (half-height) and minimum value. For all cluster sizes, the center of the singularity spectrum α_0 demonstrates monotonic decrease with increase of α_p (Fig. 30B), till reaching saturation.

Observing Figures 30B and 31A it is clear that dependency of α_0 and $\Delta\alpha$ on α_p changes with the size of the cluster. Thus, finite-size scaling technique was used to collapse the curves and to generate universal, size independent curves. The crossing point of the curves, i.e. $\alpha_{p_c} = 0.07$ was adopted here as the critical point (recall that α_p here plays the role of temperature). Following the order parameter and response function analogy, the scaling was reached through the magnetization scaling function, $M = L^{-\beta/\nu} g_M(tL^{1/\nu})$, and susceptibility scaling function $\chi = L^{\lambda/\nu} g_\chi(tL^{1/\nu})$.

On Figures 30C and 31B we show results of finite-size scaling, collapsing the curves for α_0 and $\Delta\alpha$, for clusters of different sizes, onto universal curves, independent of size. The scaling was accomplished for $\nu = 3/2$, $\gamma = 0.24$ and $\beta = 0.0$, wherefrom one may
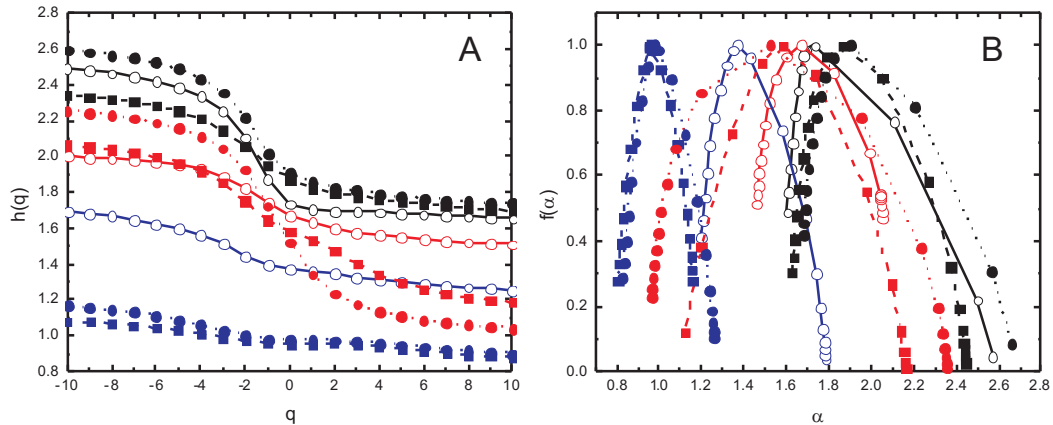
Figure 29: Plots of (A) the generalized exponent $h(q)$ determined as the slope of the linear regression between $log(\ell)$ and $log[Fq(\ell)]$ and (B) the singularity spectra $f(\alpha)$ for different values of α_p and cluster size. Black, red and blue colors correspond to α_p equal to 0.01, 0.07 and 1.0, respectively; open circle, closed square and closed circle correspond to clusters formed by 2,000, 10,000 and 50,000 particles.

conclude that the system undergoes a second order phase transition near $\alpha_{p_c} = 0.07$ with an ordered phase at $\alpha_p < 0.07$ and disordered phase at $\alpha_p > 0.07$.

5.3.2 Microscopic aggregation growth as a function of the "surface tension" and flow - Scenario 2 and 3

5.3.2.1 Morphological changes

Preferential flow direction of incoming particles can bring about significant effect on the resulting aggregate shape, which may be fundamental for modeling growth phenomena of structures in confined geometries, and/or in presence of external fields. Generally speaking, curvilinear force fields can produce extremely diverse and realistic (even artistic) patterns (LOMAS, 2012), but a comprehensive understanding of cause-effect relationships in complex scenarios is still lacking.

Two simple scenarios are therefore considered in the present work (as mentioned in section 5.2.1) with a bias in a single direction (while the other three directions are equiprobable), and with bias in two directions. Resulting clusters of a large number of simulations for different values of probabilities ρ_1 and ρ_2, as well as different values of sticking pro-

Number of Particles	Maximum	90% of maximum	Average point	Minimum
A 2000	$\alpha_p = 0.01$ $\alpha_0 = 1.82$	$\alpha_p = 0.04$ $\alpha_0 = 1.64$	$\alpha_p = 0.16$ $\alpha_0 = 1.35$	$\alpha_p = 0.51$ $\alpha_0 = 0.88$
10000	$\alpha_p = 0.01$ $\alpha_0 = 1.88$	$\alpha_p = 0.05$ $\alpha_0 = 1.69$	$\alpha_p = 0.12$ $\alpha_0 = 1.39$	$\alpha_p = 0.40$ $\alpha_0 = 0.90$
50000	$\alpha_p = 0.01$ $\alpha_0 = 1.91$	$\alpha_p = 0.06$ $\alpha_0 = 1.72$	$\alpha_p = 0.08$ $\alpha_0 = 1.42$	$\alpha_p = 0.24$ $\alpha_0 = 0.93$
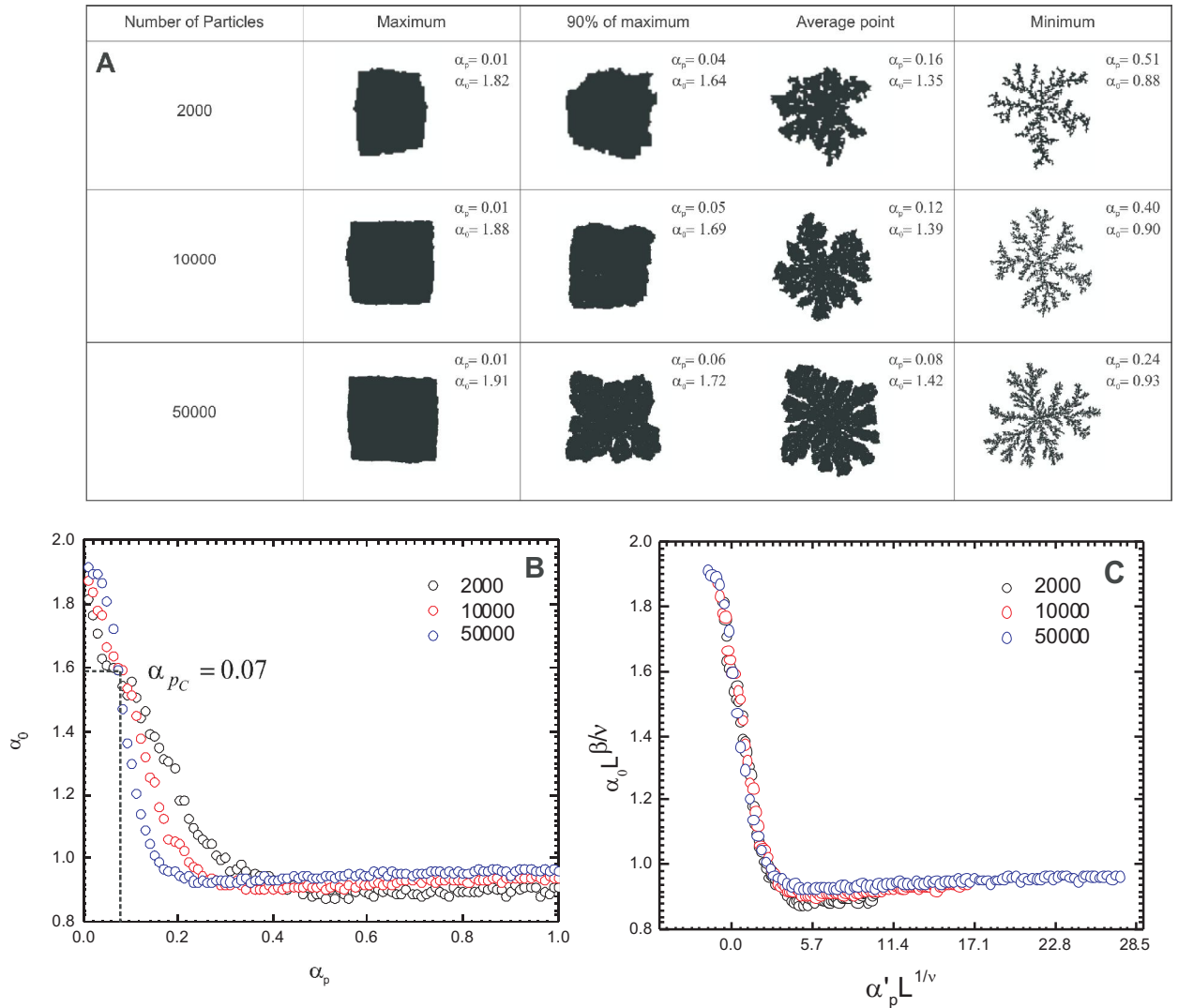
Figure 30: Multifractal properties of the perimeter fluctuations of clusters of different sizes L (2000, 10000 and 50000 particles) obtained from the generalized DLA model preposed by Batchelor and Henry (1992). (A) Sample images of the growing structures for different cluster sizes, and different α_p values from reference points of the plot of B. (B) Average maximum point of the multifractal spectra, α_0, as a function of the "surface tension" parameter α_p for different cluster sizes. The collapse (C) of the curves in B was achieved for the critical exponents $\beta = 0.0$ and $\nu = 1.5$ ($\alpha_p' = \alpha_p - \alpha_{p_c}$).

bability α_p (surface tension) are displayed in Figs. 32 and 33, where a wide spectrum of shapes can be observed. As may be expected, generally speaking the aggregates obtained in these scenarios tend to grow more rapidly in the direction of the increased incoming flux, yielding anisotropic clusters.

Besides, the higher the probability of a preferable direction, the less spread turns out the aggregate, with no influence in the formation of branches, but the type of the branches
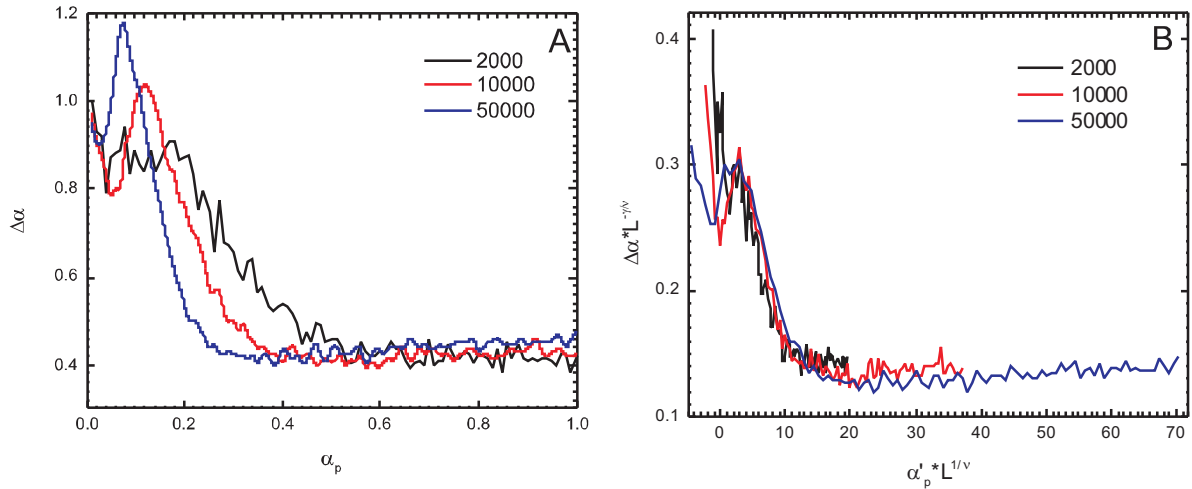
Figure 31: (A) Average width of the multifractal spectrum, $\triangle\alpha$, as a function of the "surface tension" parameter α_p for different cluster sizes. The collapse of these curves (B) was achieved for the critical exponents $\gamma = 0.24$ and $\nu = 1.5$ ($\alpha_p^{'} = \alpha_p - \alpha_{p_c}$).

and the surface of the cluster turn out to be different when the fluxes increase. Broader branches and more compact surface (but not in totally) are observed for higher fluxes, converging to a BD-like aggregate. This occurs because the growth probability inside the cluster increases as the particles lose the natural motion and go straight in some direction, such as the effect of a magnetic field or a low density environment.
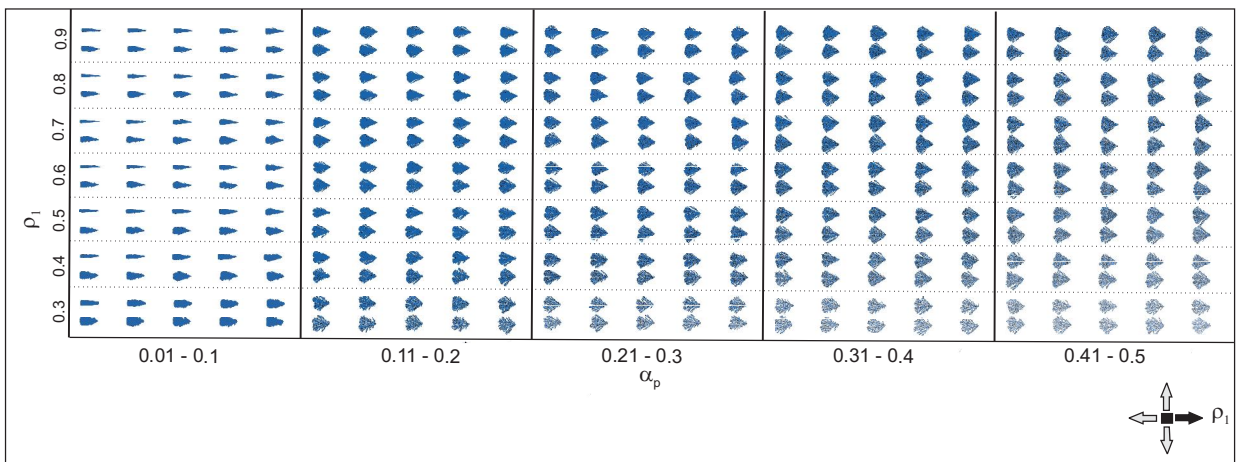
Figure 32: Morphological diagram of clusters with 50,000 particles aggregated for different α_p (x axis) and flow, ρ_1 (y axis)

However, the branch formation and roughness still more related with α_p, i.e. the way that particles aggregate, since branches are only observed for cluster with α_p higher than

0.1. The results for scenario 3 (control of the fluxes in two perpendicular directions) turned out very similar to the previous scenario, except to the fact that asymmetric shapes are obtained when the two probabilities are different (Fig. 33).
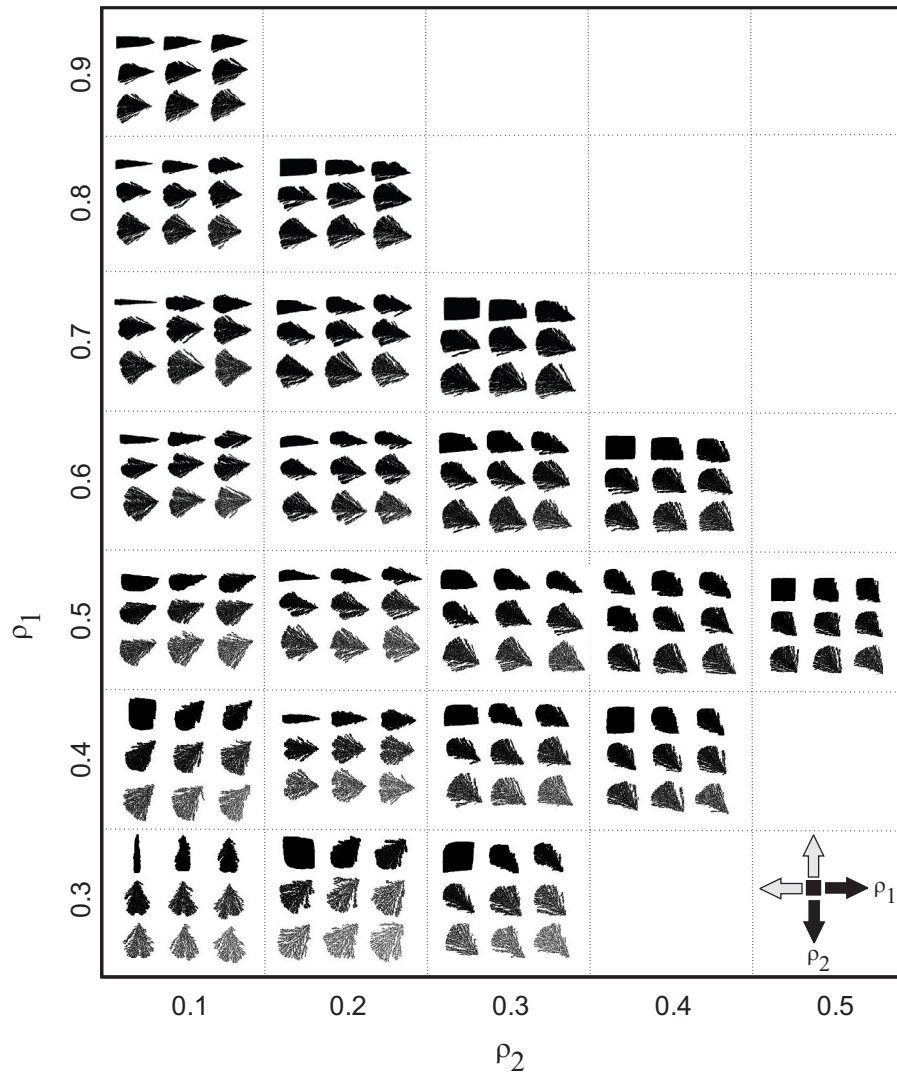
Figure 33: Morphological diagram of clusters with 50,000 particles aggregated for different α_p and flow, ρ_1 (left to right) and ρ_2 (up to down)

The influence of particle flow in the resulting shapes during growth process has been extensively discussed in the literature for two calcareous structures, fish otoliths and stony corals. Wu et al. (2011) showed experimentally that hydrodynamic effects inside the inner ear controls the particle motion from a Brownian motion to cilia-driven flow, and the otolith self-assembly is related to this balance of motion and the particle localization in solution. Pronounced anisotropy of fish otholits (that is rather common) may therefore be attributed to different growth probabilities of sites exposed to the flux of incoming particles, as cor-

roborated with the simulations performed in the present work. The similarity between the simulated aggregates and real fish otholits is highlited in Figure 34, which strongly suggests that flux may be one of the most important factors that control the overall shape of otholits.
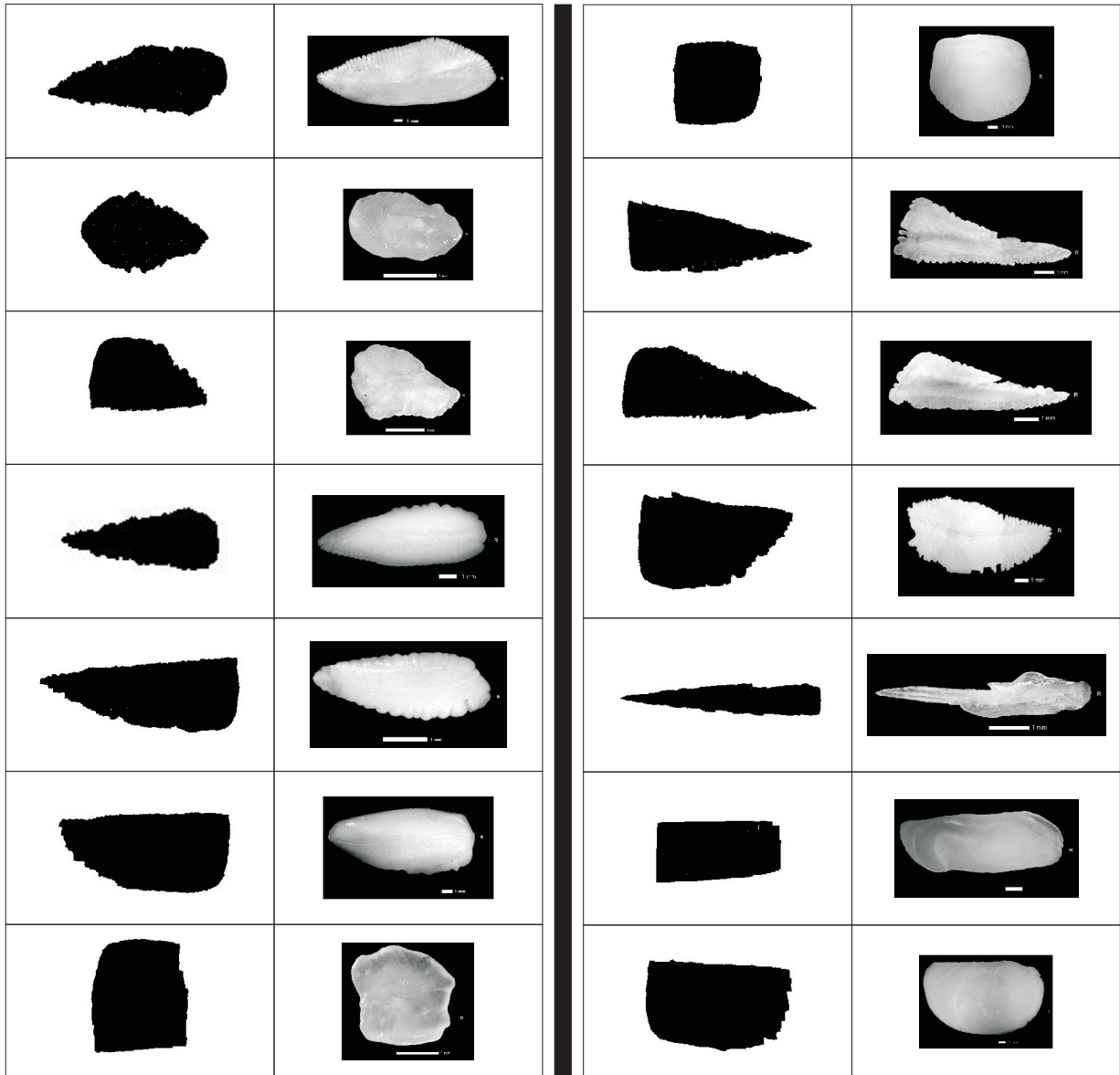
Figure 34: Schematic representation of the similarity between artificial cluster (50,000 particles) obtained in the present work (scenarios 2 and 3) and fish otoliths.

In the case of stony corals, several papers have discussed the influence of flow and nutrients concentration in branch formation for branched species, based on Laplacian growth (KAANDORP et al., 1996; MERKS et al., 2003) and, more recently, on independent polyp growth (MERKS et al., 2004). However, the level of influence of flow on coral growth is still not well understood. Merks et al. (2003) concluded that branch formation is spontaneous in their

Laplacian-based growth model and the compactness of the corals depends on the ratio of the rates of growth and nutrient transport. In a subsequent work, the same authors stated that the spacing of polyps influences the thickness of branches and the overall compactness. On the other hand, the results obtained by the present DLA generalization model indicate that branch formation in the simulated clusters depends primarily on the surface tension (α_p), and the thickness of branches and the overall compactness depends on both surface tension and flow.

5.3.2.2 Multifractal properties

In Figure 35 the singularity spectra are displayed for several combinations of values of the sticking probability α_p (surface tension) and several values of the directional bias probability (flux) ρ_1. It is seen that higher flux values result in more compact and smoother structures, shifting the multifractal spectrum to the right (Fig. 35B). However, as can be seen from Fig. 36A, this effect is only significant fro α_p values close to critical value of 0.07, when protrusions and cavities start to appear in the clusters. The flux increases the growth probability in these parts, and consequently the surface compactness is also increased. For values of ρ_1 higher than 0.6 and at high surface tension, the flux has almost no effect. Similar situation is observed when two direction motion probabilities are controlled (ρ_1 and ρ_2), as high probabilities always present higher α_p values, and saturation is achieved at high surface tension (no significant effect of the flux is observed) (Fig. 37).

Beside the fact that a preferable motion direction permits that particles reaches deeper sites, the growth probability also increases due to directional bias that the flux imposes to the cluster growth. In practice, if a particle reach the cluster, but does not stick to it, the chance to return and try again at the same position till the adhesion occurs increases with the flux.

The flux effect is noted not only in the α_0 parameter (position of the spectrum), but also in the width of the spectrum (Fig35 and Fig. 36B-D). The multifractal spectra of clusters with flux higher than 0.3 are wider for both small and large scales, as indicated by the red region
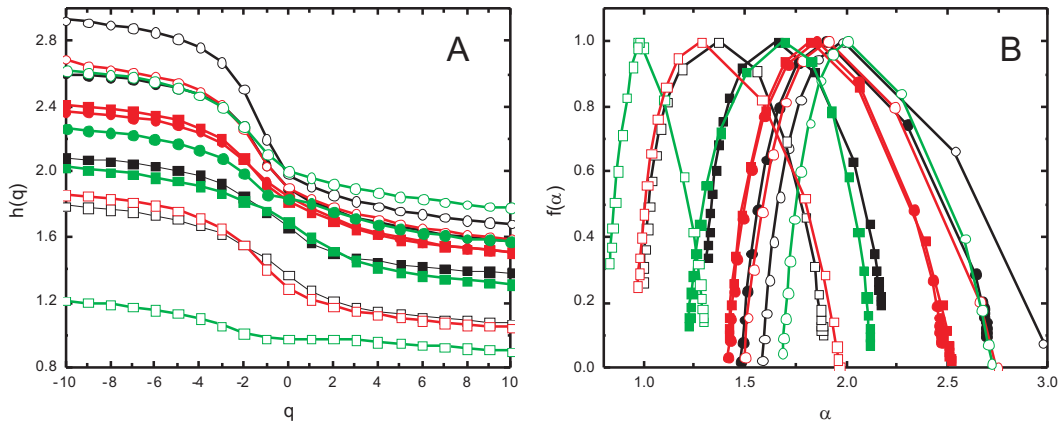
Figure 35: Plots of (A) the qth moment versus the generalized exponent $h(q)$ determined as the slope of the linear regression between $log(\ell)$ and $log[Fq(\ell)]$ and (B) the singularity spectra $f(\alpha)$ for different values of "surface tension" ($\alpha_p = 0.01$ - open circle; $\alpha_p = 0.05$ - closed circle; $\alpha_p = 0.1$ - closed square; and $\alpha_p = 0.5$ - open square) and flux ($\rho_1 = 0.9$ - black; $\rho_1 = 0.6$ - red; and $\rho_1 = 0.3$ - green).

in Figures 36B-D. Furthermore, around $\rho_1 = 0.3$ the multifractal spectrum width parameter distributions ($\Delta\alpha$, $\Delta\alpha-$ and $\Delta\alpha+$) lose the point of maximum, becoming monotonic functions of α_p and ρ_1.

Similar behavior is observed in simulation of the Ising model considering the influence of a magnetic field. In this model, the magnetic field decreases the magnitude of the susceptibility peak for finite systems, while in the thermodynamic limit presence of a finite field destroys the singularity at the transition point (STANLEY, 1971). This represents a further analogy with magnetic phase transitions, and a further indication that the multifractal parameters α_0 can be treated as a order parameter and $\Delta\alpha$ as response function, while α_p plays the role of temperature.

5.3.3 Microscopic aggregation growth as a function of the "surface tension" and particle concentration- Scenario 4

5.3.3.1 Morphological changes

In the previous scenarios, the particles were released from an uniform random position on the circle that envelopes the cluster. In the present case, a pre-defined locations was
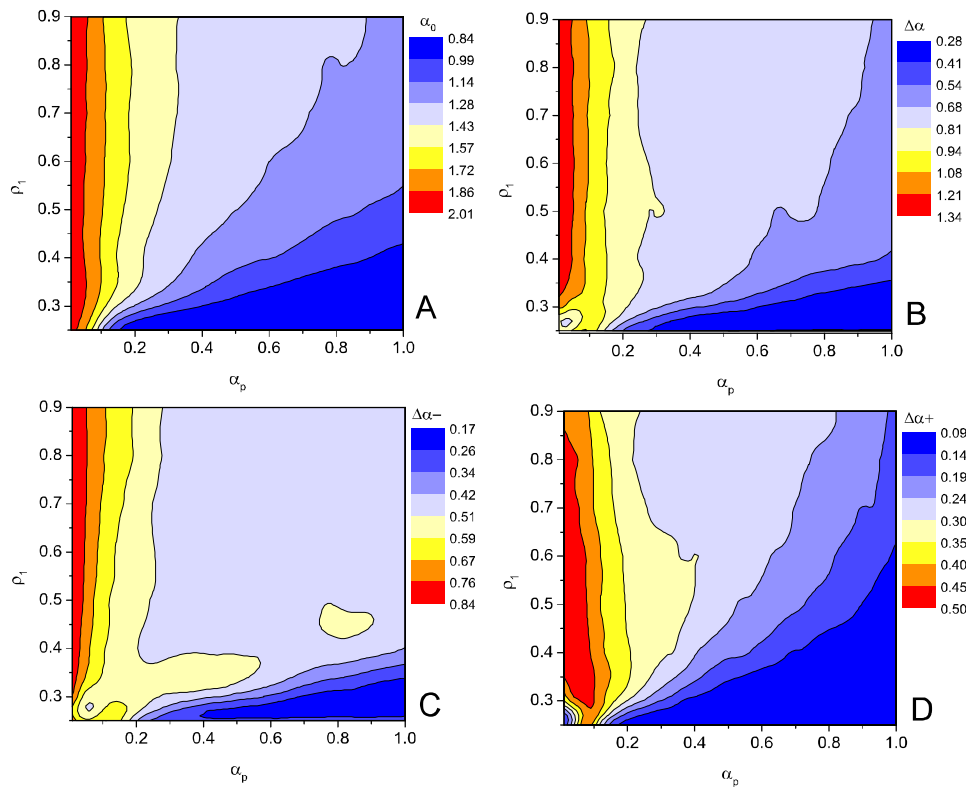
Figure 36: Phase diagram of the four multifractal parameters determined from the aggregates contour fluctuations in function of different "surface tension" (α_p) and flux (ρ_1). (A) α_0, position of the maximum of $f(\alpha)$, corresponding to $q = 0$; (B) $\Delta\alpha$, the width of the spectrum, estimate of the range of α where $f(\alpha) > 0$, obtained by $\Delta\alpha = \alpha_{max} - \alpha_{min}$; (C) $\Delta\alpha-$, the contribution of the negative part of q in the spectrum range, estimated by $\Delta\alpha- = \alpha_{max} - \alpha_0$; and (D) $\Delta\alpha+$, the contribution of the positive part of q in the range of the spectrum, estimated by $\Delta\alpha+ = \alpha_0 - \alpha_{min}$.

used ($\mu = 3\pi/2$ and $\mu = 5\pi/4$), where a von Mises distribution (equivalent of a Gaussian, on a circle) was centered, and subsequently used in the simulations as the source for generating particles. The choice of these locations was significant for the visual appearance of the final shape of the clusters, square for $\mu = 3\pi/2$ (270°) and oblique for $\mu = 5\pi/4$ (225°) (Fig. 38), resulting from the fact that the square grid was used in the simulations (see the schematic illustration on Figure 39). More precisely, for low α_p values, if an uniform random position is used, the resultant shape is a square (Fig. 25); in the case of the first location, the resultant shape is the side of the square; and the vertex of the square is obtained for the second location.

Figure 37: Phase diagram of the multifractal parameter α_0 determined from the aggregates contour fluctuations in function of different "surface tension" (α_p) and fluxes (ρ_1 and ρ_2).

In turn, wider shapes and more developed secondary branches (in the case of high "surface tensions") are observed for lower κ values (i.e. lower concentration of particles), as a strategy to find more resources necessary for the growth process. Such behavior is observed in specimens of stony corals (Fig. 40), where specimens that grew in a sheltered site present more open branched structure than those species that are collected from an exposed site (MERKS et al., 2003). However, the particle concentration per se does not significantly change the shape of the aggregates, similar to the effect of the flux magnitude. Perhaps, a combination of both the directional bias in movement and the concentrated particle source could generate more irregular shapes.
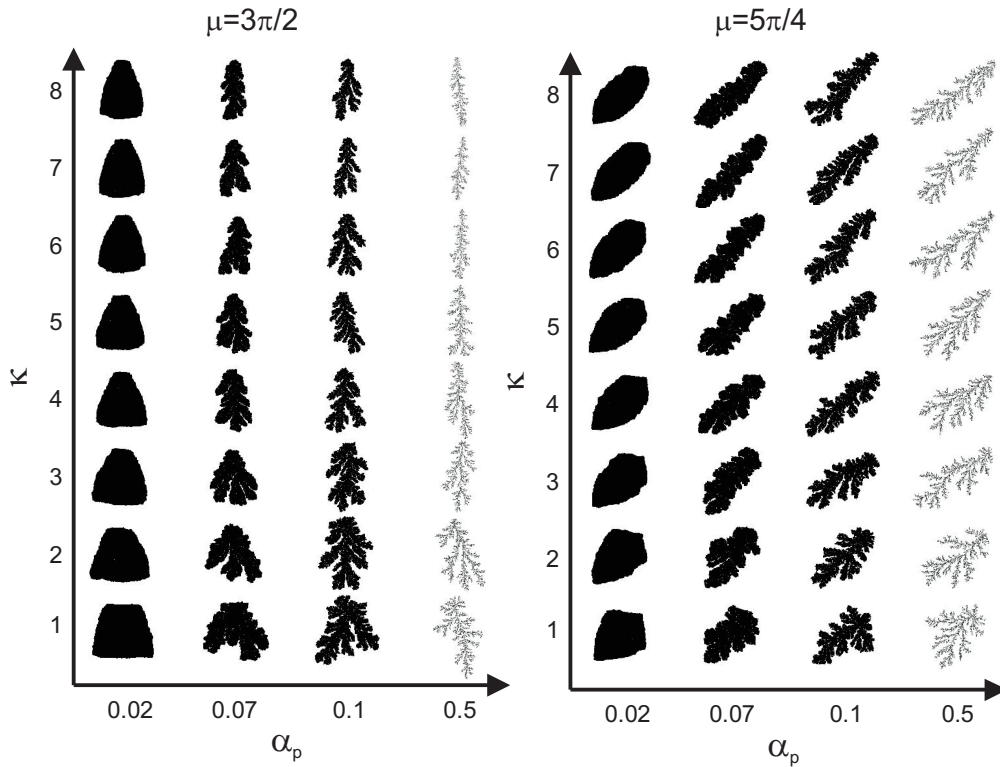
Figure 38: Morphological diagram of clusters with 50,000 particles aggregated under different "surface tension" (α_p) and particles concentration (κ), considering the two central location (μ) of the particle releasing distribution.
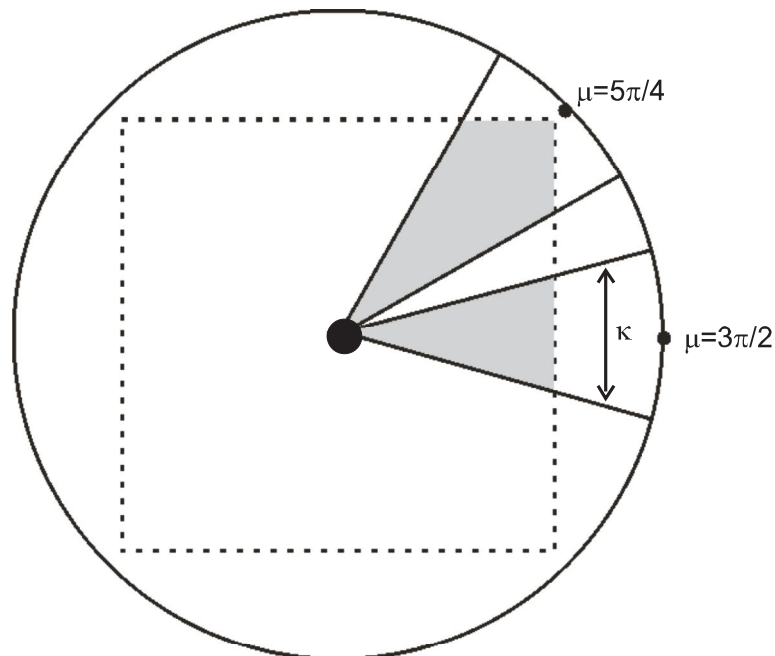
Figure 39: Schematic representation of the location parameter (μ) effect on the cluster growth in response of a square grid. κ is the concentration parameter of the von Mises distribution used to choose the site of the circle which the particle is released.
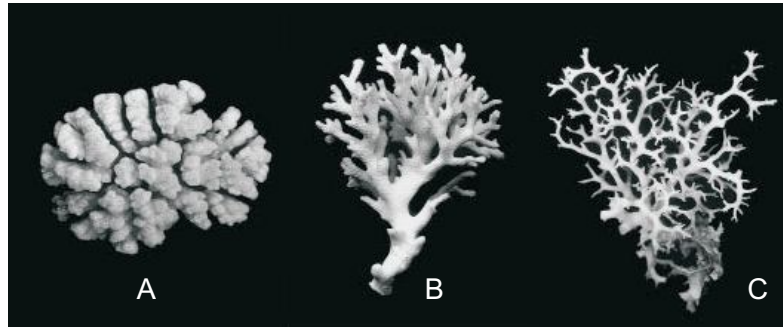
Figure 40: Growth forms of the stony coral *Pocillopora damicornis* (from Kaandorp *et al*, 1996; original from Veron and Pichon, 1976). Form (A) originates from an exposed site, (B) from a semiprotected site, and (C) from a site sheltered from water movement.

5.3.3.2 Multifractal properties

Concerning the cluster contour characteristics, the multifractal parameters present slight differences among locations and particle concentrations (Fig. 41). In contrast with the flux, α_0 and $\Delta\alpha$ do not depend on the two particle distribution parameters, showing similar behavior of that for scenario 1, where a monotonic decrease was observed for α_0 as a function of α_p till saturation is reached for high "surface tensions" (Fig. 41A and B). Also, the maximum of α_0 at $\alpha_p = 0.07$ (the critical "surface tension") was observed for all parameter location and particle concentrations (Fig. 41C and D) . However, the concentration affect the cluster contour fluctuation that growth at low α_0 (≤ 0.05) in minor scales, i.e. for negative q (Fig. 41E and F). In other words, the more spread the cluster becomes, the more irregularities in small scales it presents.
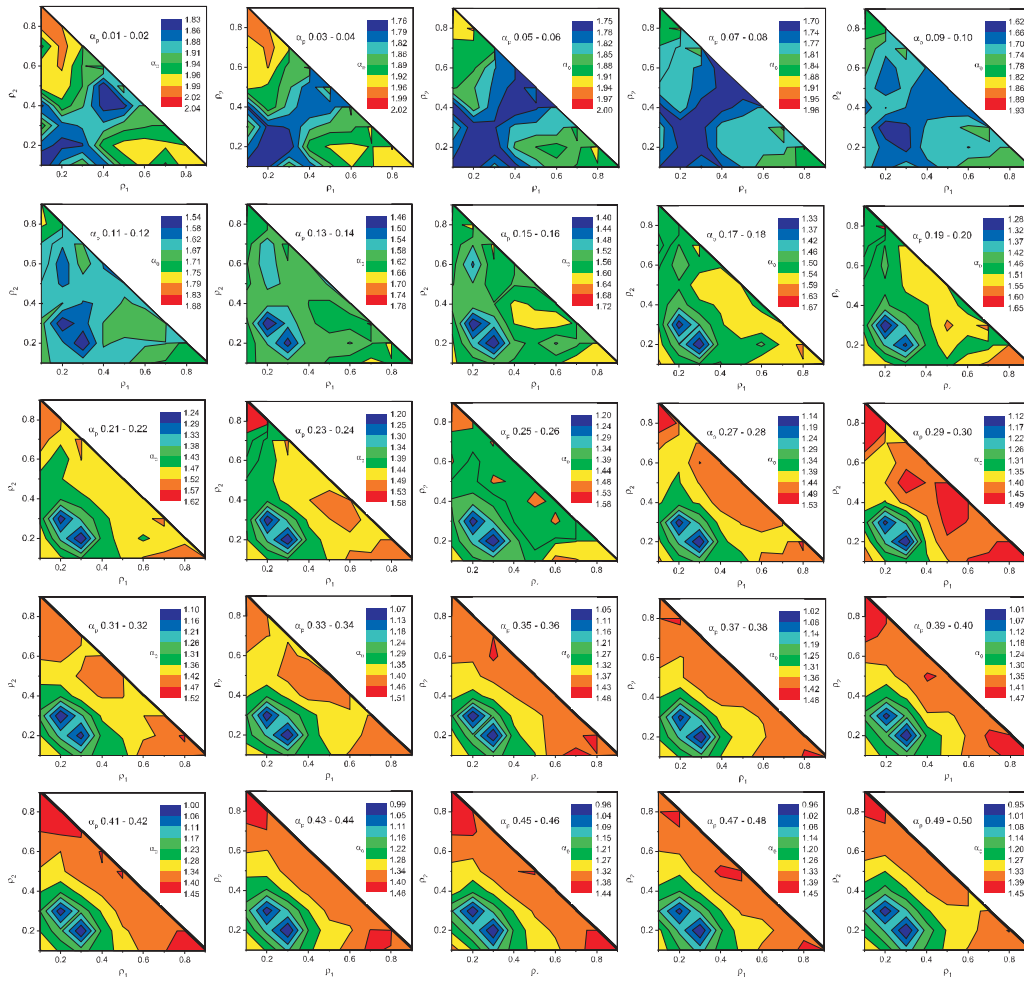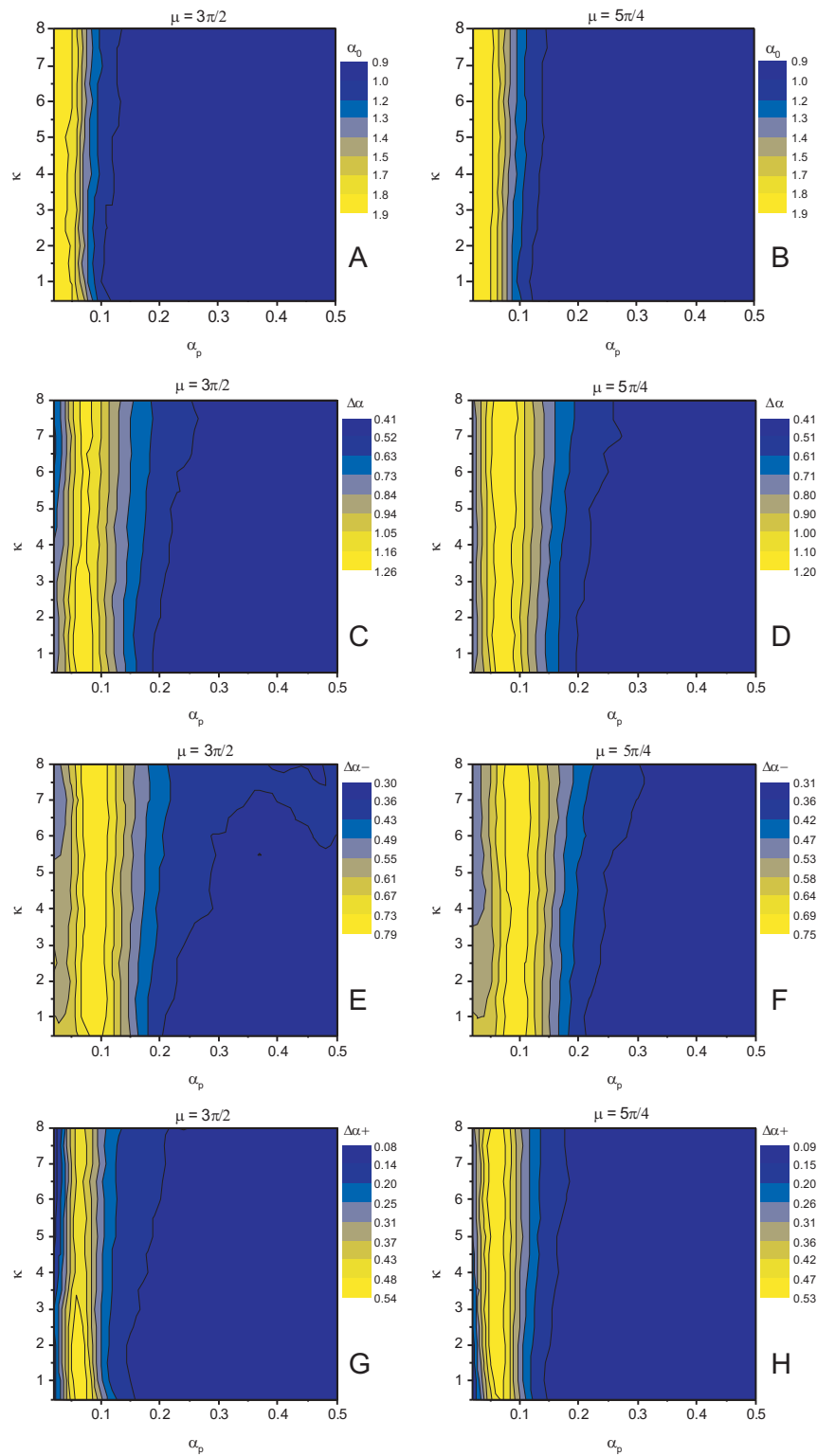
Figure 41: Phase diagram of the four multifractal parameters determined from the aggregates contour fluctuations in function of different "surface tension" (α_p) and the concentration parameter (κ) for the two angular location ($\mu = 2\pi$ and $\mu = \pi/4$). (A and B) α_0, position of the maximum of $f(\alpha)$, corresponding to $q = 0$; (C and D) $\Delta\alpha$, the width of the spectrum, estimate of the range of α where $f\alpha(\alpha) > 0$, obtained by $\Delta\alpha = \alpha_{max} - \alpha_{min}$; (E and F) $\Delta\alpha-$, the contribution of the negative part of q in the spectrum range, estimated by $\Delta\alpha- = \alpha_{max} - \alpha_0$; and (G and H) $\Delta\alpha+$, the contribution of the positive part of q in the range of the spectrum, estimated by $\Delta\alpha+ = \alpha_0 - \alpha_{min}$.

6   General Conclusions

The multifractal analysis of closed contours through "The Traveling Observer" MF-DFA has shown to be very promising. The results presented here indicate that this novel approach can capture intrinsic characteristics of the growth process hidden in the contour fluctuations, that are reflected by the multifractal parameters. In fact, these parameters can be used as shape descriptors in classification problems, as an interface to other traditional quantitative methods employed for shape analysis (see. chapter 4). However, their interpretation goes far beyond simple shape classification. For instance, in chapter 3, multifractal parameters were related to alteration of metabolic rate between reproduction and somatic growth of fishes, reflected in the otolith growth process, and they can be used to determine length and age of first maturity. In turn, the parameter behavior observed in chapter 5 demonstrates strong resemblance with classical phase transitions, showing properties not yet observed for a microscopic aggregation model.

The use of the contour radius normalized by the zero-th harmonic to extract the fluctuations appears to be one of the most important advantages of this new method. First, this characteristic makes the results invariant to size. This represents an important feature when shape classification is being conducted, and it has turned capable of removing the finite-size effects on the multifractal spectrum of DLA, previously observed in other works.

Furthermore, this procedure takes into account only the "active zone" of growing, and works as a measure of growth probability of this zone. This characteristics can be used to model the variation of a boundary of a natural structure during its growth, as a picture of the boundary condition (such as "surface tension" and flux) at a certain time (such as fish

age) or locality, reflected on the multifractal parameters. Possibly, multifractal parameters may be used as input ingredients for future microscopic growth otolith models, reflecting the degree of heterogeneity of aggregation probability.

The morphological results presented in chapter 5 suggest that the use of the generalized DLA model, in combination with multifractal analysis of the contour fluctuations, represents a potential approach to model the growth of otoliths. In the present work, applying only simple modifications on "surface tension", flux and particle concentration, artificial shaped-otoliths were obtained, with a stronger contribution of flux and "surface tension". However, during otolith biomineralization, there are other genetic and environmental mechanisms that could control the otolith morphogenesis and, hence, the isotropy or anisotropy of calcium aggregation around the otolith perimeter. These mechanisms include the shape of the inner ear (GAULDIE, 2000), proteins (PAYAN et al., 1999; SÖLLNER et al., 2003), and discontinuities of the otolith growth provoked by stimulus to the macula due to environmental conditions (LECOMTE-FINIGER, 1999; CARDINALE; DOERING-ARJES; GANGNON, 2004). Due to the characteristic of being easily generalized, these factors could be simulated as an extension of the generalized DLA model described here, allowing the measurement of individual factor contributions.

Because our current approach is somewhat general, it could be applied to contour studies of other natural structures. For example, the multifractality of mineral particles has been assessed only in terms of their spatial arrangement in soil (POSADAS et al., 2003; XIE et al., 2010), and such a shape characterization would also be important in the classification of different types of sediment (DROLON; DRUAUX; FAURE, 2000) and ash particles (DELLINO; LIOTINO, 2002). How the multifractal properties of contour fluctuations behave during particle formation, and how they relate to geological processes, is still not well understood, and the current "travelling observer" MF-DFA approach may prove useful for the elucidation of such phenomena.

References

ALLEMAND, D. et al. Fish otolith calcification in relation to endolymph chemistry. In: E. BAÜERLEIN. **Handbook of Biomineralization: Biological Aspects and Structure Formation**. Weinheim: Wiley/VCH, 2007. cap. 7, p. 291–308.

BARABÁSI, A.-L.; STANLEY, H. E. **Fractal Concepts in Surface Growth**. Cambridge: Cambridge University Press, 1995.

BATCHELOR, M.; HENRY, B. Growth and form in the zero-noise limit of discrete laplacian growth processes with inherent surface tension: I. the square lattice. **Physica A**, v. 187, p. 551–574, 1992.

BERENS, P. A matlab toolbox for circular statistics. **Journal of Theoretical Biology**, v. 31, n. 10, p. 1–21, 2009.

BRANKOV, J. G. **Introduction to Finite-Size Scaling**. Leuven: Leuven University Press, 1996.

CAMPANA, S. E. Chemistry and composition of fish otoliths: pathways, mechanisms and applications. **Marine Ecology Progress Series**, v. 188, p. 263–297, 1999.

CARDINALE, M.; DOERING-ARJES, P.; GANGNON, P. Effects of sex, stock, and environment on the shape of known-age atlantic cod (*Gadus morhua*) otoliths. **Canadian Journal of Fisheries and Aquatic Science**, v. 61, p. 158–167, 2004.

CHHABRA, A.; JENSEN, R. V. Direct determination of the $f(\alpha)$ singularity spectrum. **Physical Review Letters**, v. 62, p. 1327–1330, 1989.

COMMITTEE ON CMMP 2010, SOLID STATE SCIENCES COMMITTEE, NATIONAL RESEARCH COUNCIL. **Condensed-Matter and Materials Physics: The Science of the World Around Us**. Washington: The National Academies Press, 2007.

DAMOURAS, S. et al. An empirical examination of detrended fluctiation analysis for gait data. **Gait and Posture**, v. 31, p. 336–340, 2010.

DELLINO, P.; LIOTINO, G. The fractal and multifractal dimension of volcanic ash particles contour: a test study on the utility and volcanological relevance. **Journal of Volcanology and Geothermal Research**, v. 113, p. 1–18, 2002.

DROLON, H.; DRUAUX, F.; FAURE, A. Particles shape analysis and classification using the wavelet transform. **Pattern Recognition Letters**, v. 21, p. 473–482, 2000.

DUARTE-NETO, P. et al. The use of sagittal otoliths in discriminating stocks of common dolphinfish (*Coryphaena hippurus*) off northeastern brazil using multishape descriptors. **ICES Journal of Marine Science**, v. 65, p. 1114–1152, 2008.

EDEN, M. A two-dimensional growth process. In: NEYMAN, J. (Ed.). Berkeley: University of California Press, 1961. p. 223–239.

FEDER, J. **Fractals**. New York: Plenum Press, 1988.

FERNÁNDEZ, E. et al. Are neurons multifractals? **Journal of Neuroscience Methods**, v. 89, p. 151–157, 1999.

FORBES, C. et al. **Statistical Distributions**. New Jersey: Wiley, 2011.

GAULDIE, R. W. Function, form and time-keeping properties of fish otoliths. **Comparative Biochemistry and Phisiology A**, v. 91, n. 2, p. 395–402, 2000.

GAULDIE, R. W.; CRAMPTON, J. S. An eco-morphological explanation of individual variability in the shape of the fish otolith: comparison of the otolith of *Hoplostethus antlanticus* with other species by depth. **Journal of Fish Biology**, v. 60, p. 1204–1221, 2002.

GAULDIE, R. W.; NELSON, D. G. A. Aragonite twinning and neuroprotein secretion are the cause of daily growth rings in fish otoliths. **Comparative Physiology and Biochemistry**, v. 90A, p. 501–506, 1988.

GILDEN, D. L.; SCHMUCKLER, M. A.; CLAYTON, K. The perception of natural contour. **Psychological Review**, v. 100, n. 3, p. 460–478, 1993.

GREEN, B. S. et al. **Tropical Fish Otoliths: Information for Assessment, Management and Ecology**. New York: Springer, 2009.

HANAN, W. G.; HEFFERNAN, D. M. Geometrical multifractality of the perimeter of dla clusters. **Chaos, Solitons and Fractals**, v. 12, p. 193–195, 2001.

_____. Multifractal analysis of the branch structure of diffusion-limited aggregates. **Physical Review E**, v. 85, p. 021407, 2012.

HARTE, D. **Multifractals : Theory and Applications**. Boca Raton: Chapman and Hall/CRC, 2001.

IVANOV, P. C. et al. Multifractality in human heartbeat dynamics. **Physical Review Letters**, v. 389, p. 461–465, 1999.

JOHNSON, K. **A diffusion-limited aggregation (DLA) cluster. Copper aggregate formed from a copper sulfate solution in an electrode position cell**. 2006. Available at: `http://en.wikipedia.org/wiki/File:DLA_Cluster.JPG`. Accessed on May 19th, 2012.

JOLIVIET, A. **Compréhension des mécanismes de Biominéralisation: quantification spatialisée des fractions minérale et organique et influence de facteurs environnementaux**. Tese (Doutorado) — Ecole Doctorale des Sciences de la Mer, Institut Universitaire Européen de la Mer, Plouzané, France, 2009.

KAANDORP, J. A. et al. Effect of nutrient diffusion and flow on coral morphology. **Physical Review Letters**, v. 77, n. 11, p. 2328–2331, 1996.

KANTELHARDT, J. W. **Encyclopedia of Complexity and Systems Science**: Fractal and multifractal time series. New York: Springer, 2009.

KANTELHARDT, J. W. et al. Multifractal detrended fluctuation analysis of nonstationary time series. **Physica A**, v. 316, p. 87–114, 2002.

LAM, C.-H. Finite-size effects in diffusion-limited aggregation. **Physical Review E**, v. 52, n. 3, p. 2841–2847, 1995.

LECOMTE-FINIGER, R. L'otolithe: la boîte des téléostéens. **Année**, v. 38, p. 107–122, 1999.

LESTREL, P. E. Introductio and overview of fourier descriptors. In: P. E. LESTREL. **Fourier Descriptors and Their Applications in Biology**. Cambridge: Cambridge University Press, 1997. cap. 2, p. 22–44.

LOMAS, A. **Aggregation: Complexity out of Simplicity**. 2012. Available at: `http://www.andylomas.com/sketch_0087_final.pdf`. Accessed on November 2, 2012.

LOMBARTE, A. et al. A web-based environment for shape analysis of fish otoliths. **Scientia Marina**, v. 70, p. 147–152, 2006.

LOMBARTE, A.; POPPER, A. N. Quantitative analysis of postembryonic hair cells addition in the otolith endorgans of the inner ear of the eurpean hake, merllucius merllucius (gadiformes, teleostei). **Journal of Comparative Neurology**, v. 345, p. 419–428, 1994.

LOPES, R.; BETROUNI, N. Fractal and multifractal analysis: a review. **Medical Image Analysis**, v. 13, p. 634–649, 2009.

MANDELBROT, B. Stochastic models for the earth's relief, the shape and fractal dimension of coastlines, and the number area rule for islands. **Proceedings of the National Academy of Sciences USA**, v. 72, n. 10, p. 2825–2828, 1975.

MEAKIN, P. **Fractals, Scaling and Growth Far from Equilibrium**. Cambridge: Cambridge University Press, 1998.

MEAKIN, P.; FAMILY, F.; VICSEK, T. Viscous fingering simulated by off-lattice aggregation. **Journal of Colloid and Interface Science**, v. 117, n. 2, p. 394–399, 1987.

MELLON-DUVAL, C. et al. Growth of european hake (*Merluccius merluccius*) in the gulf of lions based on conventional tagging. **ICES Journal of Marine Science**, v. 67, p. 62–70, 2010.

MéNARD, F. et al. Climatic oscillations and tuna catch rates in the indian ocean: a wavelet approach to time series analysis. **Fisheries Oceanography**, v. 16, n. 1, p. 95–104, 2006.

MERKS, R. et al. Models of coral growth: spontaneous branching, compactification and the laplacian growth assumption. **Journal of Theoretical Biology**, v. 224, p. 153–166, 2003.

MERKS, R. M. H. et al. Polyp oriented modelling of coral growth. **Journal of Theoretical Biology**, v. 228, n. 3, p. 559–576, 2004.

MONTEIRO, L. R. et al. Allometric changes and shape differentiation of sagitta otoliths in sciaenid fishes. **Fisheries Research**, v. 74, p. 288–299, 2005.

MUGIYA, Y. Phase difference between calcification and organic matrix formation in the diurnal growth of otoliths in the rainbow trout, *Salmo gairdneri*. **Fishery Bulletin**, v. 85, p. 395–401, 1987.

MUKKAMALA, S. B.; ANSON, C. E.; POWELL, A. K. Modelling calcium carbonate biomineralisation processes. **Journal of Inorganic Biochemistry**, v. 100, p. 1128–1138, 2006.

MURGUÍA, J. S.; URÍAS, J. On the wavelet formalism for multifractal analysis. **Chaos**, v. 11, n. 4, p. 858–863, 2001.

MUZY, F.; BACRY, E.; ARNEODO, A. Wavelets and multifractal formalism for singular signals: Application to turbulence data. **Physical Review Letters**, v. 67, n. 25, p. 3515–3518, 1991.

NAGATANI, T. Multifractal structures of mass and growth probability distributions in difusion-limited aggregation on hierarchical lattices. **Physical Review A**, v. 38, n. 5, p. 2632–2640, 1988.

NOLF, D. Otolith piscium. In: HANS-PETER SCHULTZE. **Handbook of Paleoichthyology**. New York: Cambridge University Press, 1985. p. 145 pp.

OSWIECIMKA, P.; KWAPIEN, J.; DROZDZ, S. Wavelet versus detrended fluctuation analysis of multifractal structures. **Physical Review E**, v. 74, p. 016103, 2006.

PARISI-BARADAD, V. et al. Otolith shape contour analysis using affine transformation invariant wavelet transforms and curvature scale space representation. **Marine and Freshwater Research**, v. 56, p. 795–804, 2005.

PAYAN, P. et al. Chemical composition of saccular endolymph and otolith in fish inner ear: lack of spatial uniformity. **American Journal of Physiology**, v. 277, n. 1, p. R123–131, 1999.

PENG, C.-K.; BULDYREV, S. V.; HAVLIN, S. Mosaic organization of dna nucleotides. **Physical Review E**, v. 49, n. 2, p. 1685–1689, 1994.

PICKOVER, C. A. **The Math Book: From Pythagoras to the 57th Dimension, 250 Milestones in the History of Mathematics**. New York: Sterling, 2009.

PIERA, J. et al. Otolith shape feature extraction oriented to automatic classification with open distributed data. **Marine and Freshwater Research**, v. 56, p. 805–814, 2005.

PIÑEIRO, C.; SAÍNZA, M. Age estimation, growth and maturity of the european hake (*Merluccius merluccius* (linnaeus, 1758)) from iberian atlantic water. **ICES Journal of Marine Science**, v. 60, p. 1086–1102, 2003.

PLISCHKE, M.; RÁCZ, Z. Active zone of growing clusters: Diffusion-limited aggregation and the eden model. **Physical Review Letters**, v. 53, n. 5, p. 415–418, 1984.

PONTON, D. Is geometric morphometrics efficient for comparing otolith shape of different fish species? **Journal of Morphology**, v. 267, p. 750–757, 2006.

POPPER, A. N.; HOXTER, B. The fine structure of the sacculus and lagena of a teleost fish. **Hearing Research**, v. 5, p. 245–263, 1981.

POSADAS, A. N. D. et al. Multifractal characterization of soil pore systems. **Soil Science Society of America Journal**, v. 67, p. 1361–1369, 2003.

RECASENS, L.; CHIERICONI, V.; BELCARI, P. Spawning pattern and batch fecundity of the european hake (*Merluccius merluccius* (linnaeus, 1758)) in the western mediterranean. **Scientia Marina**, v. 72, p. 721–732, 2008.

SANTANA, F. M. et al. Otolith micro- and macrostructure analysis to improve accuracy of growth parameter estimation for white mullet *Mugil curema*. **Aquaic Biology**, v. 7, p. 199–206, 2009.

SEURONT, L. **Fractals and multifractals in ecology and aquatic science**. Boca Raton: CRC Press, 2010.

SÖLLNER, C. et al. Control of crystal size and lattice formation by starmaker in otolith. **Science**, v. 302, p. 282–286, 2003.

STANLEY, H. E. **INTRODUCTION TO PHASE TRANSITIONS AND CRITICAL PHENOMENA**. Oxford: CLARENDON PRESS, 1971.

STOSIC, T.; STOSIC, B. D. Multifractal analysis of human retinal vessels. **IEEE Transactions on Medical Imaging**, v. 25, p. 1101–1107, 2006.

STRANSKY, C. Geographic variation of golden redfish (*Sebastes marinus*) and deep-sea redfish (*S. mentella*) in the north atlantic based on otolith shape analysis. **ICES Journal of Marine Science**, v. 62, p. 1691–1698, 2005.

TéL, T.; FÜLÖP, A.; VICSEK, T. Determination of fractal dimensions for geometrical multifractals. **Physica A**, v. 159, p. 155–166, 1989.

TéL, T.; VICSEK, T. Geometrical multifractality of growing structures. **Journal of Physics A: Mathematical and Theoretical**, v. 20, p. L835–L840, 1987.

THOMPSON, D. W. **On Growth and Form**. [S.l.]: Canto, 1992.

TRACEY, S. R.; LYLE, J. M. Application of elliptical fourier analysis of otolith form as a tool for stock identification. **Fisheries Research**, v. 77, p. 138–147, 2006.

VICSE, T.; FAMILY, F.; MEAKIN, P. Multifractal geometry of diffusion-limited aggregates. **EUROPHYSICS LETTERS**, v. 12, n. 3, p. 227–222, 1990.

VICSEK, T. **Fractal Growth Phenomena**. Singapore: World Science Publishing, 1989.

WILSON, R. R. Depth related changes en sagitta morphology in six macrourid fishes of the pacific and atlantic oceans. **Copeia**, p. 1011–1017, 1985.

WORTHMAN, H. A. Relação entre o desenvolvimento do otólito e o crescimento do peixe no auxílio na distinção de populações de pescada (*Plagioscion squamosissimus*). **Acta Amazônica**, v. 9, p. 573–586, 1979.

XIE, H.; WANG, J.-A.; KWAśNIEWSKI, M. A. Multifractal characterization of rock fracture surfaces. **International Journal of Rock Mechanics and Mining Sciences**, v. 36, p. 19–27, 1999.

XIE, S. et al. Assessing microstructures of pyrrhotites in basalts by multifractal analysis. **Nonlinear Processes in Geophysics**, v. 17, p. 319–327, 2010.

Appendix A

6.1   The von Mises Distribution

The von Mises distribution is analogue to a normal distribution on the line (FORBES et al., 2011). Here, x is a circular random variate, with range $0 < x \le 2\pi$. The parameters of this distribution are: the concentration (scale) parameter $\kappa > 0$ and the location parameter (mean direction and mode) $0 \le \mu < 2\pi$, analogous to the mean and variance in the normal distribution. Its distribution function is

$$F(x|\mu,\kappa) = [2\pi I_0(\kappa)]^{-1} \left\{ x I_0(\kappa) + 2\sum_{j=0}^{\infty} I_j(\kappa) \frac{sin\,[j(x-\mu)]}{j} \right\} \tag{6.1}$$

where $I_t(\kappa) \sum_{i=0}^{\infty} \frac{(\kappa^2/4)^t}{i!\Gamma(t+i+1)}$ is the Bessel function of order t; for order $t=0$, $I_0(\kappa) \sum_{i=0}^{\infty}(\kappa^{2i}/[2^{2i}(i!)^2])$. Then, the probability density function (pdf) is defined as

$$f(x|\mu,\kappa) = \frac{e^{\kappa cos(x-\mu)}}{2\pi I_0(\kappa)} \tag{6.2}$$

A uniform distribution of a rectangular variate between a and b is obtained in the limit of small κ:

$$lim_{\kappa \to 0} f(x|\mu,\kappa) = U(x), \tag{6.3}$$

with $\mu = 0$, $\kappa = 2\pi$, and pdf $1/(2\pi)$. The von Mises variate tends to a normal variate in the limit of large κ:

$$lim_{\kappa \to \infty} f(x|\mu,\kappa) = \frac{exp\left[\frac{-(x-\mu)^2}{2\sigma^2}\right]}{\sigma\sqrt{2\pi}}, \tag{6.4}$$

with $\mu = 0$, and $\sigma = 1/\kappa$

The maximum likelihood estimates of the parameters μ and κ are, respectively, $\hat{\ell}(\mu|x) = tan^{-1}\left(\sum_{i=1}^{n} sinx_i / \sum_{i=1}^{n} cosx_i\right)$, and $\hat{\ell}(I_1(\kappa)/I_0(\kappa)|x) = \frac{1}{n}\left[\left(\sum_{i=1}^{n} cosx_i\right)^2 \left(\sum_{i=1}^{n} sinx_i\right)^2\right]^{1/2}$.

6.2   The von Mises Random Angle Generator

For the simulation performed in chapter 5, random angles from a von Mises distribution were obtained basing on the Matlab code included in a Matlab Toolbox for Circular Statistics (BERENS, 2009). The C code version is the follow:

```
double fi;
vonmise(&fi);


int vonmise(double *random){


int  i, sign;
double a,b,r;
double u[3],z,f,c,x,y;


a = 1 + sqrt((1+4*k*k));
b = (a - sqrt(2*a))/(2*k);
r = (1 + b*b)/(2*b);


*random=0;


while(1){
for(i=0;i<3;i++){
u[i]=(double)UNI/RMAX;
}
z = cos(PI*u[0]);
f = (1+r*z)/(r+z);
c = k*(r-f);
if(u[1]< (c * (2-c)) || !(log(c)-log(u[1])+1-c<0))break;
```

```
}

if((u[2]-0.5)>0)sign=1;

else if((u[2]-0.5)<0)sign=-1;

else sign=0;

*random = mi+sign*acos(f);

y=sin(*random);

x=cos(*random);

*random=atan2(y,x);

return 1;

}
```